UiO : Department of Physics
University of Oslo

Inline Electron Holography

- Theoretical and Experimental Aspects

Heine H. Ness

M.Sc. Thesis, Spring 2018

Inline Electron Holography

—

Theoretical and Experimental Aspects

Heine Håland Ness

M.Sc. Thesis in Materials, Energy and Nanotechnology

Department of Physics

University of Oslo

May 2018

Supervisors:

Assoc. Prof. Øystein Prytz & M.Sc. Tarjei Bondevik

2018

Inline Electron Holography - Theoretical and Experimental Aspects

Heine Håland Ness

http://www.duo.uio.no/

Print: Reprosentralen, University of Oslo

Acknowledgements

This thesis is submitted as art of the masters degree in Materials Science and Nanotechnology by the Departement of Physics at the University of Oslo. The work has been preformed in association with the Structure Physics (Strukturfysikk).
I would like to express my gratitude to my two supervisors Øystein Prytz and Tarjei Bondevik, for their guidance, invaluable help and motivation.
I also want to thank Christoph T. Koch for his teachings and advice. Furthermore I would like to thank Phuong D. Nguyen, Holm Krimse and Domas Birenis for their teaching, and I would like to thank Johan Taftø for fruitful scientific discussions.
In addition i would like to thank all the wonderful members of both Structure Physics group and Solid State Electrochemistry (FAstStoff Elektrokjemi (FASE)) group for creating the best possible environment; scientifically and socially. And a special thanks to the people of the Structure Research and Electron Microscopy group (SEM) of the Humboldt University, for giving me an enjoyable stay, and providing priceless advice and guidance. And I gratefully acknowledge the NORTEM project for providing the financial support allowing me to travel abroad.
I also have to thank all the MEAN 2013 people, this achievement would not have been possible without you. And, a special thanks to my office mate, Sindre R. Bilden for always looking on the bright side of life.
Thanks my parents Vigdis and Hjalmar for their never ending support, and to my brother Sigbjørn, and my sister Frøya, thanks for cheering me on.

Heine H. Ness

Abstract

With ever decreasing size of electronics the need study of sub micrometer structures is prominent. The transmission electron microscope (TEM) gives the possibility to study structures at the nano scale. One technique that the TEM enables is inline electron holography, whith this technique, the electrostatic potential of a material can be found. By using a defocus series of electron micrographs, the full electron wavefunction may be recovered by simulating the processes that take place in the TEM. The phase of the electron wavefunction holds information of the potential experienced by the electron wave.

In this thesis, we study a state of the art inline electron holography technique, titled Full Resolution Wave Reconstruction (FRWR). A review of the reconstruction algorithm is given, and we have tested the FRWR capabilities to recover the mean inner potential of Cu_2O, and the potential profile across a Cu_2O/CuO/ZnO heterojunction. In addition the effects of experimental setup such as objective aperture and energy filtering have been investigated. Furthermore, theoretical values of the mean inner potential have been calculated from following two different models, a non-binding atom model and an ionized atom model.

The theoretical values for the mean inner potential of Cu_2O was found to be 17.29 V for a non-binding model and 12.78 V for an ionized atom model, whereas the experiential values was estimated to be 15.46$\pm$2.18 V.

For the Cu_2O/CuO interface, the theoretical calculations gave a potential of 3.13 V and 2.34 V for the non-binding and ionic models, respectively. The experimental value was 1.33$\pm$0.70 V. The CuO/ZnO transition gave theoretical values of 3.14 V for the non-binding model and 2.34 V for the ionic model, and an experimental value of 2.60$\pm$0.84 V.

Contents

Acknowledgements **iii**

Abstract **v**

1 Introduction and motivation **1**

2 Crystallography and Wave properties **3**

2.1 Definition of the crystal lattice 3

2.1.1 Laue conditions and the reciprocal lattice 4

2.1.2 Bragg's law and TEM 4

2.1.3 Small angle approximation 5

2.2 Waves and Scattering 6

2.2.1 Coherence 7

2.2.2 Wave particle duality 9

2.2.3 The double slit experiment for electrons 10

2.3 Huygens-Fresnel principle 11

2.3.1 Kinematical scattering 11

2.3.2 The structure factor 12

2.4 Scattering factors 13

3 Crystal Potential **15**

3.1 The mean of a periodic potential 15

3.1.1 Mean inner potential from scattering factors 16

3.2 The mean inner potential effect on fast electrons 19

3.2.1 Derivation of the phase shift 21

3.2.2 Additional effects of the potential 24

4 Finding the electron phase **27**
4.1 The phase problem 27
4.2 Gabor's electron holography 28
4.2.1 Off-axis holography 29
4.2.2 Inline electron holography 31
4.2.3 Transport of intensity equation 33

5 Full Resolution Wave Reconstruction **37**
5.1 The Full Resolution Wave Reconstruction algorithm 37
5.1.1 The coherent transfer function 38
5.1.2 The defocus-spread-dependent envelope function 43
5.1.3 Aperture function 45
5.1.4 Partial spatial coherence envelope 45
5.1.5 The detector and its point spread function 46
5.2 Describtion of the FRWR algorithm 48
5.2.1 Image alignment 50
5.2.2 Transport of intensity equation in FRWR 52
5.2.3 Gradient flipping of the phase 54

6 Experimental results and discussion **55**
6.1 Experimental details 55
6.1.1 Experimental setup 55
6.1.2 FRWRsetup tool 56
6.1.3 FRWR reconstructions 56
6.2 Samples used in this thesis 57
6.3 Investigation of the importance of the objective aperture 57
6.4 Effect of energy filtering in the mean inner potential measurements of Cu_2O 62
6.5 Measurements of potentials in a Cu_2O/CuO/ZnO heterojunction 68

7 Conclusions and suggestions for future work **77**

Appendices **79**

A Measuring the Objective aperture size **81**

B Measuring the modulation transfer function **83**

C Energy Filtered Transmission Electron Microscopy **85**

D The log ratio method for thickness measurements **89**

Bibliography **90**

Chapter 1

Introduction and motivation

With the ever decreasing size of electronics, the need to study sub micrometer structures is on the rise. There are several different methods available, each specialized in its own way. However, there is one method in particular that distinguish itself from the rest. The transmission electron microscope (TEM) enables for the study of nanometer structures. By the use of diffraction and converged beam electron diffraction the reciprocal space may be mapped and hence the real space general structure may be found. By the use of scanning electron microscopy the interpretation of sub nanometer atomic arrangement is made possible. With X-ray dispersive spectrometry, the general atomic composition may be revealed. Electron energy loss spectroscopy enables the analysis of the chemical environment on a nanometer scale. In addition, the technique of electron holography enables for the study of the mean inner potential, strain effects and magnetic properties among others.

Holography was first invented by Dennis Gabor [1] as means to escape resolution limitations from spherical aberration caused by the objective lens. Electron holography is almost synonymous with off-axis holography, where an electric biprism in the TEM column makes it possible to retrieve the full electron wave function affected by the material under investigation. Recently, inline holography has made a comeback [2, 3], due to an increase in computing power and advances in TEM performance.

Inline holography can be used to study vastly different phenomena: from studies of electron hole gass accumulation on an interface of $LaAlO_3/SrTiO_3$ [4] to measurements of strain in an (In,Al,Ga)N alloy [5] and electrical properties of Cu(In, Ga)Se_2 defects [6].

The notion of a mean inner potential is an interesting one. That a material, with its overallcharge neutrality, still has an attractive mean inner potential for electrons is a puzzling notion. Even

more so is the fact that one might detect the electron phase, ϕ. The formulation for the intensity detected in TEM, is given by the absolute square of the complex electron wave,

$$I = |Ae^{i\phi}|^2 = A^2, \tag{1.1}$$

where the detected quantity is simply reduced to the amplitude A squared. However, de Broglie revealed that subatomic particles have a wavelength, and the double slit experiment showed that particles will interfere, even with themselves!

This thesis tries to answer how it is possible to retrieve the electron phase, by the technique of inline electron holography.

Chapter 2

Crystallography and Wave properties

In this chapter, the general concepts in crystallography for describing a crystal structure will be presented. In addition, basic properties of waves and how they interact with matter will be presented.

2.1 Definition of the crystal lattice

To understand the properties of a material it is imperative to know its structure. A crystal is defined by the translational symmetry of its structure.

By populating one of the 14 *Bravais lattices* with an atom basis, any perfect crystal structure may be fully described.

A *Bravais lattice* is a mathematical construct describing points in an infinite vector space. The space is described by the lattice vector **R**, which in turn is constructed by the *primitive lattice vectors* **a**, **b**, **c** with an arbitrary set of integers n_1, n_2 and n_3:

$$\mathbf{R} = n_1\mathbf{a} + n_2\mathbf{b} + n_3\mathbf{c}. \tag{2.1}$$

The translational symmetry of the lattice is such that any point separated by **R** is equivalent to one another.

The *basis* consists of a selection of atoms, placed in the lattice such that the combined symmetry reflects the real crystal symmetry [7]. Combined these make up 230 possible crystallographic space groups.

The primitive lattice vectors are often used to define the crystal axes, giving rise to what is known as the *primitive cell* with a volume Ω given as

$$\Omega = |\mathbf{a} \cdot \mathbf{b} \times \mathbf{c}|, \tag{2.2}$$

that will fill all space in the crystal lattice by translation of **R**. The primitive cell is unique for a given crystal structure.

2.1.1 Laue conditions and the reciprocal lattice

The *unit cell* of a crystal structure is defined as the smallest possible cell with the full symmetry. To define planes in the cell, the inverse of the integers n_1, n_2 and n_3 are defined as h, k and l, respectively, known as the *Miller indices*. This allows for the construction of a *reciprocal lattice vector* **g** given as

$$\mathbf{g} = h\mathbf{a}^* + k\mathbf{b}^* + l\mathbf{c}^*, \tag{2.3}$$

which is connected to the primitive lattice vectors by the following relations:

$$\mathbf{a}^* = 2\pi\frac{\mathbf{b} \times \mathbf{c}}{\Omega} \qquad \mathbf{b}^* = 2\pi\frac{\mathbf{c} \times \mathbf{a}}{\Omega} \qquad \mathbf{c}^* = 2\pi\frac{\mathbf{a} \times \mathbf{b}}{\Omega}.$$

The Laue condition for diffraction is when the scattered waves emanating from an object constructively interferes with each other in the reciprocal space. Then, the difference in incoming and scattering wave vector noted as $\Delta\mathbf{k}$, is equal to **g**

$$\mathbf{g} = \Delta\mathbf{k}. \tag{2.4}$$

2.1.2 Bragg's law and TEM

Bragg's law explains the phenomenon of diffraction. It is based on the simple notion of two atom planes, separated by a distanse d, elastically scattering two coherent incoming waves. The geometry dictates that at a certain angle θ_B, the difference in travelling distance between the

waves scattered in the upper and lower plane is equal to some multiple integer of the wavelength λ. This leads to constructive interference between the two waves and is observed as reflections in a diffractogram.

$$2d\sin(\theta_B) = n\lambda, \tag{2.5}$$

is the famous Bragg's law connecting d, θ_B and the radiation wavelength λ.

2.1.3 Small angle approximation

For inelastic scattering, $|\mathbf{k}_0| = k_0 = 1/\lambda$ and $|\Delta\mathbf{k}| = \Delta k = 1/d$, and the connection between Figure 2.4 and equation (2.5) are

$$|\Delta\mathbf{k}| = \frac{1}{d} = \frac{2}{\lambda}\sin(\theta_B) = 2|\mathbf{k}_0|\sin(\theta_B). \tag{2.6}$$

The diffraction pattern seen on the fluorescent screen of the TEM is related to the Bragg angle (θ_B) by the small angle approximation. For a diffractogram taken at a camera length L, the distance between the central spot and a reflection, R, are related by the semi convergence angle β in the following manner,

$$\tan(\beta) = \frac{L}{R} = \frac{\lambda}{d} = 2\sin(\theta_B). \tag{2.7}$$

For $\theta_B < 1$ and $\beta < 1$, the small angle approximation is realized as

$$\tan(\beta) \approx \beta = \frac{L}{R} = \frac{\lambda}{d} = 2\sin(\theta_B) \approx 2\theta_B. \tag{2.8}$$

This is usually valid as most diffraction angles used in the TEM are within the range of 1/10 rad.

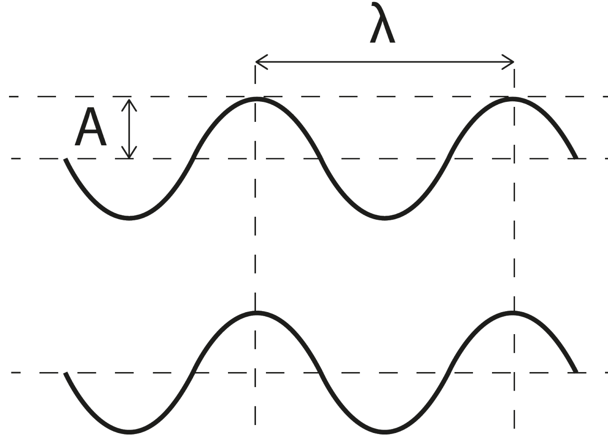

Figure 2.1: *How the amplitude A and wavelength λ is connected to a wave. The bottom wave is included to illustrate the principle of two coherent waves.*

2.2 Waves and Scattering

A wave is characterized by an oscillating nature. It has a wave peak and valley and the length from one peak to the next is defined as the wavelength, λ. The height of a peak and depth of a valley is the amplitude A, this is illustrated in Figure 2.1.

Mathematically, a wave may be represented by a sine, cosine functions, or by Euler's formula

$$e^{ip(\mathbf{r},\mathbf{k},T)} = \cos[p(\mathbf{r},\mathbf{k},T)] + i\sin[p(\mathbf{r},\mathbf{k},T)]. \tag{2.9}$$

It captures the concept of a complex wave $\Psi(\mathbf{r},\mathbf{k},T)$, where $\mathbf{r} = (x, y, z)$ is a spatial vector. A common feature of a wave is its phase $p(\mathbf{r},\mathbf{k},T) = 2\pi(\mathbf{k}\cdot\mathbf{r} - \omega T)$, containing the wave vector $\mathbf{k} = (1/\lambda_x, 1/\lambda_y, 1/\lambda_z)$. The phase $\mathbf{k}\cdot\mathbf{r}$ describes the contour of the wavefront. The term ω represent the angular frequency determined by the period i.e the time two peaks takes to pass a single point and T is time. All put together a complex wave is

$$\Psi(\mathbf{r},\mathbf{k},T) = A(\mathbf{r})e^{ip(\mathbf{r},\mathbf{k},T)} = A(\mathbf{r})e^{i(\mathbf{r}\cdot\mathbf{k})}e^{-i\omega T}. \tag{2.10}$$

The last term in eq. (2.10) involves the time and the sign is important for determining the direction that the wave moves. Through out this text the last term involving ωT will be omitted as it is easily regained by multiplying it back in to the wave function [8].

2.2.1 Coherence

If the peaks and valleys of two or more waves are located at the same position relative to each other, the waves are coherent. This is illustrated in Figure 2.1.

The intensity I_{coh} of coherent waves Ψ is represented by

$$I_{coh} = |\sum_j \Psi_j|^2, \tag{2.11}$$

capturing the interference between waves. While the intensity formed by incoherent waves I_{inc} is described by

$$I_{inc} = \sum_j |\Psi_j|^2, \tag{2.12}$$

where the intensity is constructed by individual waves that without interaction. Further discussion on the intensity is given in section 4.1.

Coherence may be divided into temporal (longitudinal) coherence and spatial (transversal) coherence. And it plays an important role in the information extracted from a TEM image, as it is directly related to the resolution limit of a microscope.

Temporal coherence

The temporal coherence in related to the energy spread of the electrons resulting in a spread in electron wavelength [9].

By viewing the electron as a wave packet the temporal coherence length is defined as the length of the wave packet along the propagation direction. If an electron beam is coherently separated and sent along two paths of different length before being overlapped, a interference pattern will emerge if the difference in path length is less than the temporal coherence length l_t. A microscope voltage V with a deviation in voltage ΔV, results in a deviation in wavelength λ of $\Delta\lambda$. Then the temporal coherence is given by

$$l_t = \frac{2V}{\Delta V}\lambda = \frac{\lambda^2}{\Delta\lambda}. \quad (2.13)$$

Spatial coherence

The spatial coherence corresponds to how well the electrons align in the plane perpendicular to the propagation direction. It depends on illumination angle of the electron source which is related to the size of the electron source.

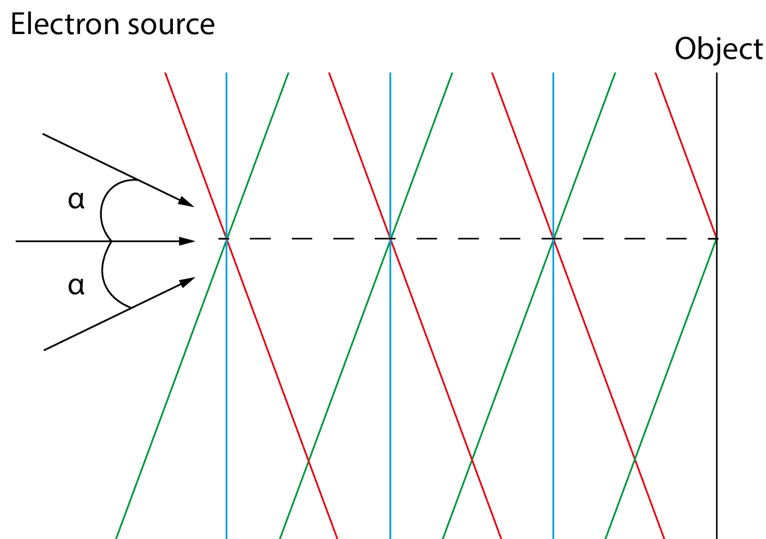

Figure 2.2: *Illustration of how the spatial stretch of the electron source gives rise to an angular deviation between electrons approaching an object.*

For waves to be spatially coherent they have to originate from the same point in space. Among available electron sources the field emission guns (FEG) have superior spatial coherency. But the FEG can not be considered as a point source, hence, the electrons are not originating from the same point. Rather, they are coming from a tiny spatial area. This implies that the electrons will have a slight angular difference (α) with respect to each other as they approach the object, as illustrated in Figure 2.2.

The spatial coherence length l_s may be expressed by the wavelength and the illumination angle as

$$l_s = \frac{\lambda}{2\alpha}. \tag{2.14}$$

The illumination angle (2α) may be reduced by inserting a condenser aperture which implies that l_s can be made arbitrary large, however, α is also restricted by the current density i and therefore the brightness [9].

2.2.2 Wave particle duality

In 1924 Louis de Broglie presented his hypothesis: that all matter have wave properties. In 1929 he recieved the Nobel prize in physics after the Clinton Davisson and Lester Germer provided evidence that proved his hypotesis [10]. The full statement that de Broglie put forward is that the momentum p of any particle of matter is equal to Plank's constant divided by its wavelength λ:

$$\lambda = \frac{h}{p}. \tag{2.15}$$

The Davisson-Germer experiment illustrated that the wavelength calculated by (2.15) corresponded to that calculated by Bragg's equation (2.5), by observing the diffraction formed by electrons reflected off the (111) face of a Ni crystal [10].

2.2.3 The double slit experiment for electrons

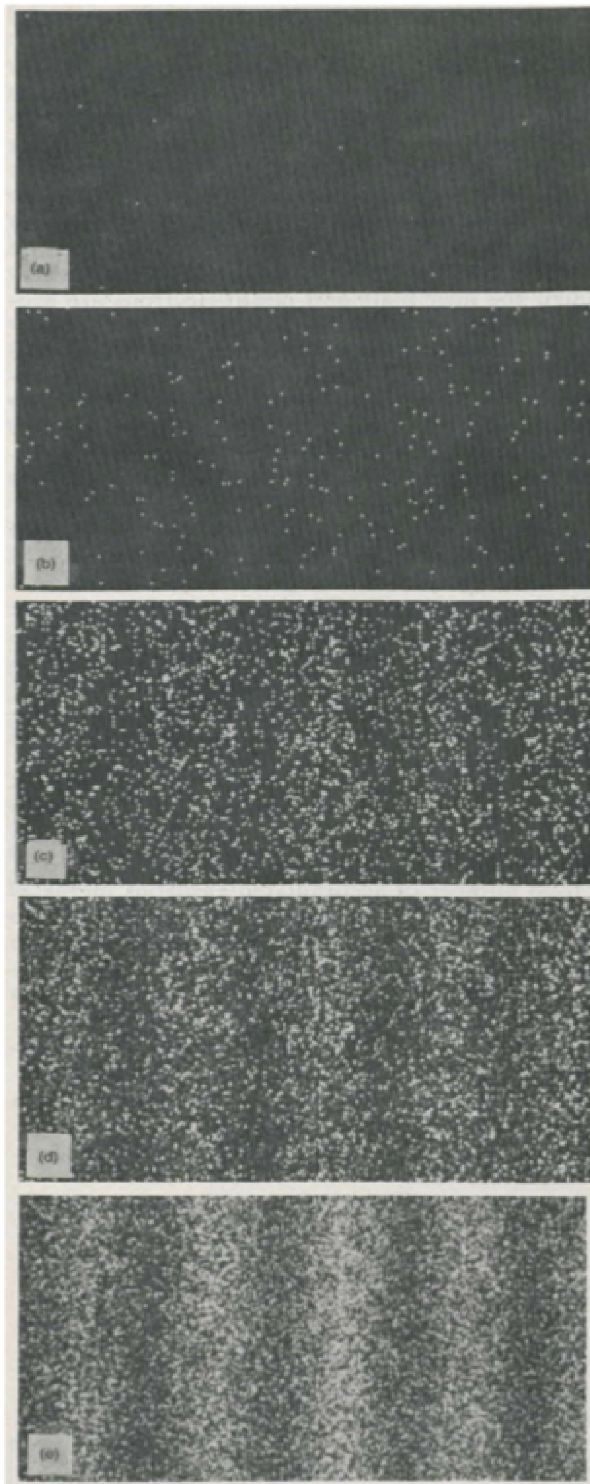

Figure 2.3: *Buildup of electron interference pattern. (a) Number of electrons = 10; (b) Number of electrons = 100; (c) Number of electrons = 3000; (d) Number of electrons = 20 000; (e) Number of electrons = 70 000. Figure taken from [11].*

In the double slit experiment, the intensity formed by coherent waves gives an interference pattern. This was first done by Thomas Young using light, thus, proving the wave nature of light.

The first to perform the double slit experiment using electrons was Tonomura et al. [11]. They used a set up with an electrostatic bi prism, which will be explained in more detail later in section 4.2.1, as a means to divide the electron path into two possible routes. By sending electrons by a large time interval and a detector that allowed for single electron detection, an image was made, built up by detecting single electrons over time. The result is showed in Figure 2.3 and clearly demonstrate a interference pattern emerging by electrons interfering with themselves. This illustrates one of the most surprising aspects of quantum mechanics and was referred to as "impossible to explain in any classical way" by Richard Feynman.

The experiment has been preformed again in recent times by Bach et al. [12]. By the use of two physical slits in a material and sending electrons through one at a time the same interference pattern is observed.

2.3 Huygens-Fresnel principle

First formulated in 1687 the Huygens-Fresnel principle states that the propagation of a wave may be described by the generation of smaller waves, called wavelets, springing out from every point in the wave front and forming the new wave front. This formulation may be used to describe any propagating wave, and it applies to both near field (Fresnel) and far field (Fraunhofer) diffraction.

Huygens-Fresnel principle connects the interpretation of scattering to the Fourier- series and transform as will be displayed in the following subsections. The scattering of an incoming electron by an arrangement of atom potentials is described by a Fourier series over all atom positions. And the Fourier coefficients are described by a Fourier transform of each individual atom potential.

2.3.1 Kinematical scattering

To describe the scattering event between an incoming electron and an atom, the Schrödinger equation must be applied. Assuming that the incoming wave is a plane wave, the scattered wave has the form of a spherical wave travelling outwards from the center of the atom, and that the distance to the detector is much larger than the scatterer. Applying the Greens function solution for the Schrödinger equation, the solution for the scattered wave $\Psi_{sc}(\Delta\mathbf{k}, \mathbf{r})$ is

$$\Psi_{sc}(\Delta\mathbf{k}, \mathbf{r}) = -\frac{2\pi m_e}{h^2}\frac{e^{i\mathbf{k}_{sc}\mathbf{r}}}{|\mathbf{r}|}\int V(\mathbf{r}')e^{-i\Delta\mathbf{k}\cdot\mathbf{r}'}d^3\mathbf{r}', \tag{2.16}$$

where h is the Planck constant, m_e the electron mass, $\mathbf{r}$ the distance from the origin of the incident wave to the detector, $\mathbf{r}'$ the distance form the origin of the incident wave to the scatterer and $\Delta\mathbf{k} = \mathbf{k}_{sc} - \mathbf{k}_0$ the difference between the incident wave vector $\mathbf{k}_0$ and the scattered wave vector $\mathbf{k}_{sc}$, as illustrated in Figure 2.4.

The total crystal potential $V(\mathbf{r}')$ in a material may be described as a sum over all potentials associated with atoms located at R_j,

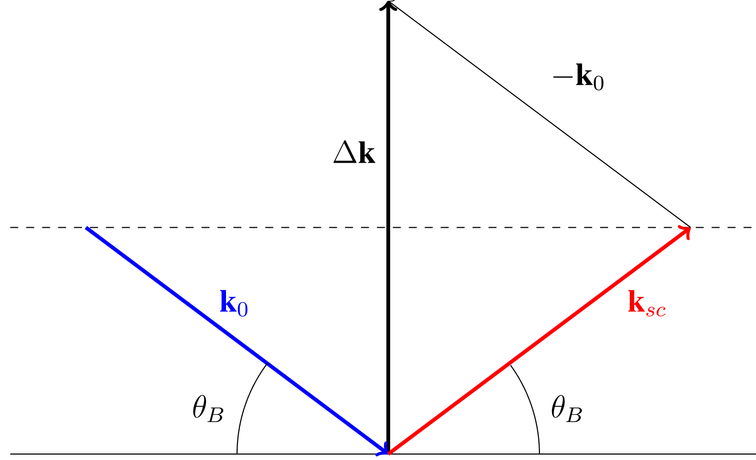

Figure 2.4: *Illustration of the difference in incoming $\mathbf{k}_0$ and scattered $\mathbf{k}_{sc}$ wave vector.*

$$V(\mathbf{r}') = \sum_{j}^{N} V_{at,j}(\mathbf{r}' - \mathbf{R}_j). \tag{2.17}$$

where N is the number of atoms in the crystal. The wave formed by the scattering from all atoms may then be formulated as a sum of wavelets emanating from each atom. This results in an expression formulated as a Fourier series over all atoms as:

$$\Psi(\Delta\mathbf{k}) = \sum_{j=1}^{N} f_j^{el}(\Delta\mathbf{k}) e^{-2\pi i \Delta\mathbf{k}\cdot\mathbf{R}_j}. \tag{2.18}$$

The Fourier coefficients $f_j^{el}(\Delta\mathbf{k})$ will be described in more detail in the following section.

2.3.2 The structure factor

By considering the crystalline material's unit cell, its structure factor F_{hkl} may be found.

$$F_{hkl} = \sum_{j} f_j^{el}(\mathbf{g}) e^{-2\pi i \mathbf{g}\cdot\mathbf{R}_j}. \tag{2.19}$$

It connects the interference of the scattering from all atoms, in the reciprocal space, thus $|F_{hkl}|^2$ is proportional to the intensity expected in a diffraction pattern.

2.4 Scattering factors

The scattering factor, $f(\Delta\mathbf{k})$, of a general object with spherical symmetry is the Fourier transform of the objects density function $\rho(\mathbf{r})$ in real space. Here, $\Delta\mathbf{k}$ is the scattering direction and $\mathbf{r}$ positions of the density.

$$f(\Delta\mathbf{k}) = \int \rho(\mathbf{r}) e^{-i\Delta\mathbf{k}\cdot\mathbf{r}} d^3\mathbf{r}. \tag{2.20}$$

For an atom, $\rho(\mathbf{r})$ is the potential affecting an incoming wave, which may be photons, electrons or neutrons. The complex exponential describes all outgoing wavelets formed by the interaction between the incoming wave and the atom, so expression (2.20) is indeed the Fourier transform of the potential. For the atomic scattering factor of electrons, $\rho(\mathbf{r})$ is the potentials associated with the atom nucleus and the electrons bound to it. Hence, the elastic electron scattering factor is

$$f^{el}(\Delta\mathbf{k}) = -\frac{2\pi m_e}{h^2} \int V_{at}(\mathbf{r}) e^{-i\Delta\mathbf{k}\cdot\mathbf{r}} d^3\mathbf{r}. \tag{2.21}$$

where m_e is the electron mass, h the Planck constant and $V_{at}(\mathbf{r})$ the full atomic potential, including all elastic electron-electron and electron-atom interactions affecting a scattered electron.

X-rays interact with the electron density of the atom and not the nucleus, and as the density describing the electron-electron interactions is characterized by the same density as x-rays. The electron scattering factor, $f^{el}(\Delta\mathbf{k})$, may therefore be formulated using the x-ray scattering factor, as

$$f^{el}(\Delta k) = \frac{mq^2}{8\pi h^2 \varepsilon_0 \Delta k^2}(Z - f^x(\Delta k)). \tag{2.22}$$

This is known as the Mott-Bethe formula. q is the elementary charge and ε_0 the vacuum permittivity.

Chapter 3

Crystal Potential

This section is dedicated to the decription of the potential of a crystal. Here the investigation and calculation of the mean inner potential in a crystalline material with periodic potential will be presented and discussed. In addition, a connection between the mean inner potential an the phase of electrons is drawn.

3.1 The mean of a periodic potential

In a crystal there exists a periodic potential $V(\mathbf{r})$ that arise from the atomic periodicity of the crystalline structure. Due to the periodic nature, it is possible to express the potential as a Fourier series. The Fourier series is constructed by a sum of plane waves over all the different wavevectors (frequencies) that reflect the periodicities of the crystal. This periodicity is given by $\mathbf{g}$, described in equation (2.3). The potential is then

$$V(\mathbf{r}) = \sum_{\mathbf{g}} V_{\mathbf{g}} e^{2\pi i \mathbf{g}\cdot\mathbf{r}}, \tag{3.1}$$

where the Fourier coefficients $V_{\mathbf{g}}$ are given by,

$$V_{\mathbf{g}} = \frac{1}{\Omega} \int_{\Omega} V(\mathbf{r}) e^{-2\pi i \mathbf{g}\cdot\mathbf{r}} d\mathbf{r}, \tag{3.2}$$

with Ω as the volume from equation (2.2). However, the shape of the crystal potential $V(\mathbf{r})$ is not known. But the shape of each individual atom potential is known, described by the scattering

factors from equation (2.4). Remembering that $\Delta\mathbf{k}$ is related to $\mathbf{g}$ allows for the replacement of the scattering factor from equation (2.21) by Fourier coefficients $V_{\mathbf{g}}$. Then, the following expression is achieved by

$$V(\mathbf{r}) = \frac{h^2}{2\pi m q \Omega} \sum_j f_j^{el}(\mathbf{g}) e^{-2\pi i \mathbf{g}\cdot\mathbf{r}_j}, \tag{3.3}$$

where the scattering factors $f_j^{el}(\mathbf{g})$ are associated with atom j of the unit cell, and m the relativistic electron mass.

Identifying its sum as the form factor

$$F_{hkl} = \sum_j f_j^{el}(\mathbf{g}) e^{-2\pi i \mathbf{g}\cdot\mathbf{r}_j}, \tag{3.4}$$

reduces the expression to

$$V(\mathbf{r}) = \frac{h^2}{2\pi m q \Omega} F_{hkl}. \tag{3.5}$$

The mean of the potential i.e. the mean inner potential (V_0), is the zeroth fourier coefficient F_{000}, and is given by

$$V_0 = \frac{h^2}{2\pi m q \Omega} F_{000}. \tag{3.6}$$

3.1.1 Mean inner potential from scattering factors

Fultz and Howe [13] have listed electron scattering factors of different elements, for accelerating voltage of 200keV, based on Rez et al. [14]. Calculations of MIP have been made for different materials based on these scattering factors, by the use of equation (3.6) and the results are displayed in Table 3.1. These results are compared to other calculated MIP provided by Kruse el al. [15], where calculations are based on scattering factors provided by Doyle and Turner [16], and Sanchez et al. [17], where the calculations are based on a self consistent analytical

atom model. Experimentally obtained MIP found in various literature are marked V_0^{exp}.

Table 3.1: *Mean inner potential calculations based on [14] for electronic scattering factors and compared to others found in the literature as described above. All results are given in units of Volt.*

Elements	V_0 by eq. (3.6)	V_0 Kruse et al. [15]	V_0 Sanchez el al. [17]	V_0^{exp}
Si	13.76	12.57	13.58	12.57 [18]
Al	16.92	-	15.71	11.90 - 15.00 [17]
Ge	15.60	14.67	13.92	15.6 [17]
NaCl	10.24	-	8.69	6.30 - 7.70 [17]
KCl	10.57	-	8.79	7.70 - 9.20 [17]
KBr	10.66	-	9.04	7.10 - 9.50 [17]
MgO	16.76	-	16.29	12.60 - 13.70 [17]
GaN	19.36	19.30	-	-
GaAs	15.38	14.19	-	14.53 [15]
ZnO	15.14	-	14.65	12.30-15.90 [17, 19]
CuO	18.27	-	-	-
Cu_2O	17.29	-	-	-

As shown in Table 3.1, the calculated MIPs varies and usually over estimates V_0 compared to the experimental results. The reason being that the calculated values are all based on the assumption of a pro crystal, that is a crystal made up of spherical non-binding atoms in the unit cell. This implies that the atoms are not bonding in the crystal, which is unphysical. The over estimation from Table 3.1 implies that binding effects the mean inner potential. The electron scattering factor which includes binding effects in the forward direction is difficult to obtain and not tabulated for ionized atoms.

However, ionized atoms do exist for x-ray structure factors and the Mott-Bethe formula connects the electron- to the x-ray scattering factor

$$f^{el}(\Delta k) = \frac{mq^2}{8\pi h^2 \varepsilon_0 \Delta k^2}(Z - f^x(\Delta k)). \tag{3.7}$$

Unfortunately, equation (3.7) tends to infinity as $\Delta k \to 0$, this poses a challenge as V_0 is calculated for forward scattering i.e. $\Delta k = 0$. As the x-ray scattering factor $f^x(\Delta k)$ is only affected by the electron cloud surrounding the atom and as $k \to 0$ it approaches the number of electrons in the cloud in a quadratic fashion. By parametrizing the x-ray structure factor $f^x(k)$ according to its shape for small k as illustrated in Figure 3.1,

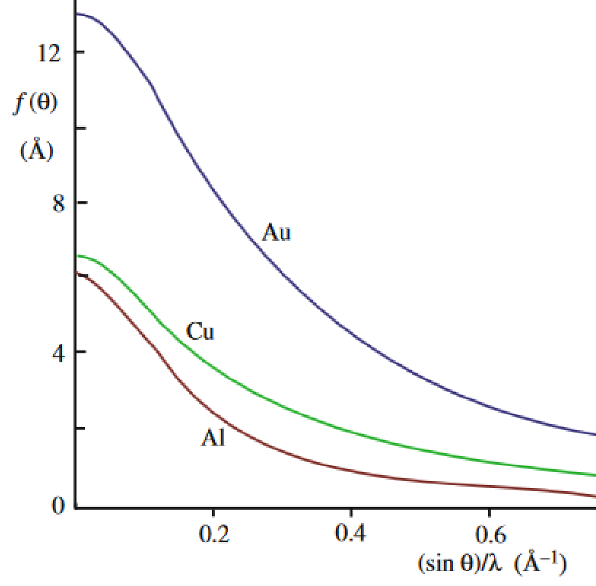

Figure 3.1: *The scattering factor $f(\theta)$ as a function of scattering angle θ for Au, Cu and Al follow a similar exponentially decay for small scattering angles. Figur taken from [13].*

$$f^x(\Delta k) = Z + n - \Delta k^2 \kappa, \tag{3.8}$$

where n is the additional- or lack of electron on the ion by being positive for anoins and negative for cations [20]. Then (3.7) becomes independent of atomic number Z as

$$f^{el}(\Delta k) = \frac{mq^2}{8\pi h^2 \varepsilon_0 \Delta k^2}(-n + \Delta k^2 \kappa). \tag{3.9}$$

Insertion into (3.3) yields

$$V_0 = \frac{q}{16\pi\varepsilon_0\Omega} \sum_j (-\frac{n_j}{\Delta k^2} + \kappa_j). \tag{3.10}$$

Due to charge neutrality the sum over n_j amounts to zero. The shape factor κ is most accurate for small k, and is defined as

$$\kappa = \frac{f^x(0) - f^x(\Delta k')}{\Delta k'^2}. \tag{3.11}$$

This leads to an alternative expression using x-ray scattering factors for ionized atoms given as

$$V_0 = \frac{q}{16\pi\varepsilon_0\Omega}\sum_j \frac{f_j^x(0) - f_j^x(\Delta k')}{\Delta k'^2}, \tag{3.12}$$

that allows for the use of the X-ray scattering factor for ionized elements and the inclusion of binding effects. To calculate V_0 from the X-ray scattering factors, $\Delta k'$ is replaced by a scattering angle close to the zero value. For all calculations made here, the closest tabulated value of $\Delta k'$ = 0,05 was chosen. Table 3.2 shows calculated V_0 by X-ray scattering factors provided by Rez et al. [14] using eq. (3.12).

Table 3.2: *Mean inner potential calculations based on [14] for X-ray scattering factors for charged atoms and compared to calculations done using electronic scattering factors. * uses Cu^+ X-ray scattering factor by [16]. All results are given in units of Volt.*

Elements	Neutral atoms by eq. (3.6)	Ionic atoms by eq. (3.12)	V_0^{exp}
NaCl	10.24	7.71	6.30 - 7.70 [17]
KCl	10.57	7.28	7.70 - 9.20 [17]
KBr	10.66	7.90	7.10 - 9.50 [17]
MgO	16.76	12.21	12.60 - 13.70 [17]
ZnO	15.14	13.08	12.30-15.90 [17, 19]
CuO	18.27	15.42	-
Cu_2O	17.29	12.78*	-

Table 3.2 suggest that including binding effects lower the calculated MIP. The two methods for calculating the MIP may be viewed as two extremes, where the first non-bonding case was modelled as a pro crystal, and the second case is a fully ionized one. The second case shows values closer to the experimental ones. However, it is still an unphysical situation as the electrons are usually redistributed throughout the unit cell due to bonding and not localized at the ions, assumed here. This illustrates that the mean inner potential is sensitive to bonding, which has also been stated by Rez et al. [14]. In addition, the calculations are strictly for bulk i.e. effects that any surfaces would have on bonding are not included.

3.2 The mean inner potential effect on fast electrons

As calculations using scattering factors has its limitations the need for a different, more direct method of finding the MIP arise. By transmitting fast electrons through a material the electron will be affected by the potential within the material. A question arises: how will the material

affect the transmitted electron?

Consider the case of two, coherent, plane electron waves travelling through vacuum, with a kinetic energy of $E_k = qV_m$, where V_m is the microscope high tension. Then one of the waves encounters an object of amorphous material that allows the wave to fully be transmitted, illustrated in Figure 3.2. The object wave will be accelerated by the potential inside the material and as there is no periodicity in an amorphous material, the potential experienced by the object wave will be the mean of the potential i.e. the MIP.

As the object wave is accelerated by the object potential its wavelength λ_{obj} will decrease, from the de Broglie relation. As the electron exits the object, it will decelerate back to its original speed, but have a change in its phase compared to the unaffected reference wave that did not experience the potential inside the object. Figure 3.2 illustrates how the object wave Ψ_{obj} is affected by the object and how the phase of the object wave is changed with respect to the reference wave Ψ_{ref}.

The claim that an electron will be accelerated by the object is based on the fact that the electron is attracted to the nucleus of an atom by the Coloumbic forces. Although electrons repel each other, the charge of a nucleus is attracting to an electron that is inside of its electron cloud as its charge not fully shielded. In this scenario $E_k = 200keV$ that corresponds to about 70% of the speed of light, by considering the electron as a particle for a moment, it has enough energy to penetrate the electron cloud of any element. This is further supported by Saldin et al. [21] that claim the electron-electron interactions diminishes with increasing energy of the incoming electron.

Assuming that the object only interact with the phase of the electron wave and that there is no loss in energy or deviation of the direction of the object wave i.e. only forward scattering, the difference in phase between the object- and reference wave is the difference in number of wavelengths that has passed the thickness, t, of the object. The phase difference $\Delta\phi$ is

$$\Delta\phi = 2\pi \left(\frac{t}{\lambda_{obj}} - \frac{t}{\lambda_{ref}} \right) = \frac{2\pi t}{\lambda_{ref}} \left(\frac{\lambda_{ref}}{\lambda_{obj}} - 1 \right). \quad (3.13)$$

In eq. (3.13) the $\frac{\lambda_{ref}}{\lambda_{obj}}$ term is equivalent to a refractive index n, by a first approximation the phase shift may be derived as the following

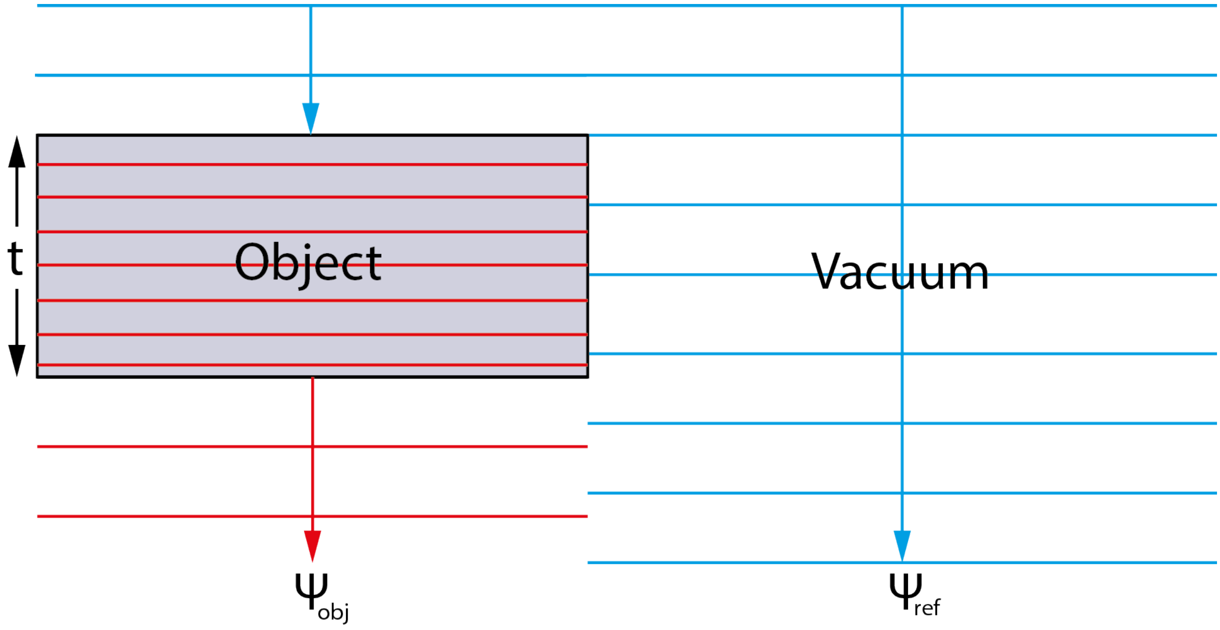

Figure 3.2: *The object wave experience a phase shift relative to a reference wave. The wavelength of the object wave is reduced due to its interaction with the potential inside an object, giving rise to the phase shift.*

$$
\begin{aligned}
\Delta\phi &= \frac{2\pi t}{\lambda_{ref}}\left(\frac{\lambda_{ref}}{\lambda_{obj}} - 1\right) = \frac{2\pi t}{\lambda_{ref}}(n-1),\\
n &= \frac{\lambda_{ref}}{\lambda_{obj}} = \frac{1/k_{ref}}{1/k_{obj}} = \frac{k_{obj}}{k_{ref}} \propto \frac{\sqrt{E_k + E_s}}{\sqrt{E_k}}\\
&= \sqrt{1 + \frac{E_s}{E_k}} \approx 1 + \frac{E_s}{2E_k},\\
\Rightarrow \Delta\phi &= \frac{2\pi t}{\lambda_{ref}}\left(1 + \frac{E_s}{2E_k} - 1\right) = \frac{\pi t}{\lambda_{ref}}\left(\frac{E_s}{E_k}\right).
\end{aligned}
$$

Here $E_s = qV_0$ where q represent the electric charge. This result gives a first approximation to the phase shift. To give a better understand the interactions between the object and electron wave a more thorough calculation is presented in the following section. This is needed as the result given here only tells of the proportionality of the phase shift.

3.2.1 Derivation of the phase shift

The wavelength may be derived from the de Broglie relation by obtaining the momentum of the electron. Starting with the known energy relation described below we get an equation for the momentum that includes E_k,

$$
\begin{aligned}
(E_0 + E_k)^2 &= E_0^2 + (pc)^2, \\
pc &= \sqrt{(E_0 + E_k)^2 - E_0^2}, \\
p &= \frac{1}{c}\sqrt{2E_0E_k + E_k^2}.
\end{aligned}
$$

$E_0 = m_0c^2$ where c the speed of light and m_0 the electron rest mass. V_m is the acceleration voltage, the kinetic energy of the electron is $E_k = qV_m$. $E_s = qV_0$ is the kinetic energy that the material adds to the object wave, where q is the electron charge and V_0 is the mean inner potential. Applying the de Broglie relation, the different wavelengths will be as follows

$$
\begin{aligned}
\lambda_{ref} &= \frac{h}{p_{ref}} = \frac{hc}{\sqrt{2E_0E_k + E_k^2}}, \\
\lambda_{obj} &= \frac{h}{p_{obj}} = \frac{hc}{\sqrt{2E_0(E_k + E_s) + (E_k + E_s)^2}}, \\
\frac{\lambda_{ref}}{\lambda_{obj}} &= \sqrt{\frac{2E_0(E_k + E_s) + (E_k + E_s)^2}{2E_0E_k + E_k^2}}, \\
&= \sqrt{\frac{2E_0E_k + 2E_0E_s + E_k^2 + 2E_kE_s + E_s^2}{2E_0E_k + E_k^2}} \\
&= \sqrt{\underbrace{\frac{2E_0E_k + E_k^2}{2E_0E_k + E_k^2}}_{=1} + \underbrace{\frac{2E_0E_s + 2E_kE_s}{2E_0E_k + E_k^2}}_{\approx 10^{-4}} + \underbrace{\frac{E_s^2}{2E_0E_k + E_k^2}}_{\approx 10^{-8}}}.
\end{aligned}
$$

A standard high tension of 200kV gives E_k = 200keV, E_0 = 0.511MeV and V_0 is usually in the range of some tens of eV. Inserting the magnitude ranges of the different values into the three terms in the square root above, results in the approximate values given. The last term is then neglected due to its relative size, which results in the following expression,

$$
\frac{\lambda_{ref}}{\lambda_{obj}} \approx \sqrt{1 + \frac{2(E_0 + E_k)E_s}{2E_0E_k + E_k^2}}.
$$

A Taylor expansion of $\sqrt{1+x}$ for $x < 1$ gives

$$\sqrt{1+x} = 1 + \frac{x}{2} - \frac{x^2}{8} + \frac{x^3}{16} - \cdots .$$

Applying the Taylor series and discarding the higher order terms results in

$$\frac{\lambda_{ref}}{\lambda_{obj}} \approx 1 + \frac{(E_0 + E_k)E_s}{2E_0E_k + E_k^2},$$

Finally, inserting into equation (3.13) yields

$$\begin{aligned}
\Delta\phi &= \frac{2\pi t}{\lambda_{ref}}\left(1 + \frac{(E_0 + E_k)E_s}{2E_0E_k + E_k^2} - 1\right) \\
&= \frac{2\pi t}{\lambda_{ref}} \frac{(E_0 + E_k)E_s}{2E_0E_k + E_k^2} \\
&= \frac{2\pi t}{\lambda_{ref}} \frac{(E_0 + E_k)q}{2E_0E_k + E_k^2} V_0.
\end{aligned}$$

The phase shift splits into three terms consisting of the thickness t, V_0, and the *interaction constant* C_E, given as

$$C_E = \frac{2\pi}{\lambda_{ref}} \frac{(E_0 + E_k)q}{2E_0E_k + E_k^2} \tag{3.14}$$

The interaction constant represents the total energy of the electrons. As the energy of the electrons increase the interaction between object and electron should decrease, this is captured by C_E. As mentioned the energy considered gives an electron a velocity close to the speed of light, so relativistic effects must be included. This is done by including the Lorentz factor $\gamma = (1 - \frac{v^2}{c^2})^{-1/2}$, which will only affect C_E.

The phase shift may then be condensed to the following expression,

$$\Delta\phi = C_E t V_0. \tag{3.15}$$

This result suggest that in the absence of diffraction and inelastic scattering, the phase shift has a linear thickness dependency.

3.2.2 Additional effects of the potential

If the object displays magnetic properties the object wave may be deflected according to the *Lorentz force*, given by

$$F_L = -q(\mathbf{v} \times \mathbf{B}), \tag{3.16}$$

where **v** is the electron velocity through a region of magnetic field **B**. This results in a deflection angle θ_L, usually in the range of μrad, given as [22]

$$\theta_L = \frac{q\lambda_{obj}}{h} B_\perp t,$$

where $B_\perp$ is the magnetic field in the plane perpendicular to the optic axis.

The Aharonov-Bohm effect [23] causes a shift in the phase despite there being no net force acting on the electron, the mere presence of a potential, magnetic or electrostatic, will effect the phase. This effect was proven by Tonomura et al. [24] for a shielded magnetic field. The phase shift imposed on a relativistic electron by the presence of electromagnetic potentials, magnetic induction component perpendicular to the object surface $\mathbf{B}_\perp$ and the MIP $V_0(\mathbf{r}_\perp, z)$, is given by [25]

$$\phi(\mathbf{r}_\perp, z) = C_E \int_t V_0(\mathbf{r}_\perp, z) dz - \frac{q}{\hbar} \int_t \int_{\mathbf{r}_\perp} \mathbf{B}(\mathbf{r}_\perp, z) d\mathbf{r}_\perp dz, \tag{3.17}$$

where $\mathbf{r}_\perp = (x, y)$ is a spatial vector in the plane parallel with the object surface.

In this thesis the main focus has been on the mean inner potential and the effects of magnetic properties have been assumed negligible as none of the materials studied have particular magnetic properties. In the absence of magnetic effects equation (3.17) reduces to

$$\phi(\mathbf{r}_\perp, z) = C_E \int_t V_0(\mathbf{r}_\perp, z) dz. \tag{3.18}$$

If V_0 does not vary with thickness the following relation between the phase and thickness reduces to

$$\phi = C_E V_0 t. \tag{3.19}$$

This gives the phase of the wave as it exits the object, and is the same expression as derived in eq. (3.15). V_0 may be retrieved by obtaining the thickness, t, of the object and the interaction constant, by the following relation

$$V_0 = \frac{\phi}{C_E t}, \tag{3.20}$$

However, by disregarding earlier assumptions of no energy lost and only forward scattering, V_0 may be complex, and is given,

$$V_0 = V' + i[V'' + V''']. \tag{3.21}$$

Here V' is the mean inner potential due to fully elastic interactions as described earlier. V'' is a potential associated with inelastic interaction, energy lost due to the interactions with the object. And V''' are connected to the scattering events causing electrons to exit the object at large angles such as diffraction effects and thermal diffuse scattering.

Chapter 4

Finding the electron phase

This chapter gives a discussion of the problems associated with experimental determination of the phase of the electron wave. Furthermore, possible solutions are presented and evaluated.

4.1 The phase problem

Due to the quantum mechanical nature of electrons, a full determination of the electron wave function is not trivial. The electron wave function is said to collapse when the electron is detected, which may be understood from the definition of the measured intensity I. It is defined as the absolute square of the electron wave function Ψ,

$$I = |\Psi|^2 = \Psi\overline{\Psi} = Ae^{i\phi}Ae^{-i\phi} = A^2, \tag{4.1}$$

hence the phase information, ϕ, is lost by observing the intensity. The complex conjugate of Ψ is represented by $\overline{\Psi}$ in the above equation. This is the phase problem.

Remembering that the phase of the wave is a relative quantity, it may still be possible to determine the phase difference to some suitable reference. If we consider the overlap of two coherent waves, the total observed intensity will be:

$$\begin{aligned} I = |\Psi_1 + \Psi_2|^2 &= (\Psi_1 + \Psi_2)\overline{(\Psi_1 + \Psi_2)} \\ &= \Psi_1\overline{\Psi_1} + \Psi_1\overline{\Psi_2} + \Psi_2\overline{\Psi_1} + \Psi_2\overline{\Psi_2}. \end{aligned}$$

By inserting a wave function $\Psi_1 = A_1 e^{i\phi_1}$ and similarly for Ψ_2, the intensity becomes

$$I = A_1^2 + A_2^2 + 2A_1 A_2 \cos(\phi_1 - \phi_2), \tag{4.2}$$

where the cosine term gives rise to the observed interference pattern of the double-slit experiment. This shows that the relative phase information may be recovered as long as there are several coherent electrons waves contributing to the intensity and thus, there may be ways of circumventing the phase problem.

4.2 Gabor's electron holography

The scenario presented in section 3.2.1, where the phase shift between an object wave and a reference wave was derived, is in many ways the premise of electron holography. In 1948, Dennis Gabor proposed a method of combating the problem of spherical aberration caused by the objective lens, which at the time was the main limiting factor for the resolution of the electron microscope.

In a letter published in Nature titled "A new microscopic principle" [1], Gabor suggested removing the objective lens altogether, relying instead on a highly coherent source to create an interference pattern between an object- and reference wave, as explained below. This shifts the limiting factor, from the objective lens to the coherence of the source.

Figure 4.1 illustrates how an electron transparent object is illuminated by an electron beam. By illuminating the object in this manner two wave fronts are created, one undisturbed, the reference wave, and on perturbed by the object, the object wave. These wave fronts will interfere some distance behind the object, and the observed interference pattern contain information about the phase and amplitude of the object wave.
This imaging technique is known as inline holography, it got its name because the limitations of the time demanded the setup to be aligned on a straight line. The term holography was coined by Gabor and is derived from greek *hòlos* meaning whole and *grapé* meaning writhing. The name is appropriate as the technique allows for the retrieval of the full object wave function, phase and amplitude, from a single image called a hologram.

By illuminating a micrograph by a light source equivalent to the original illumination the am-

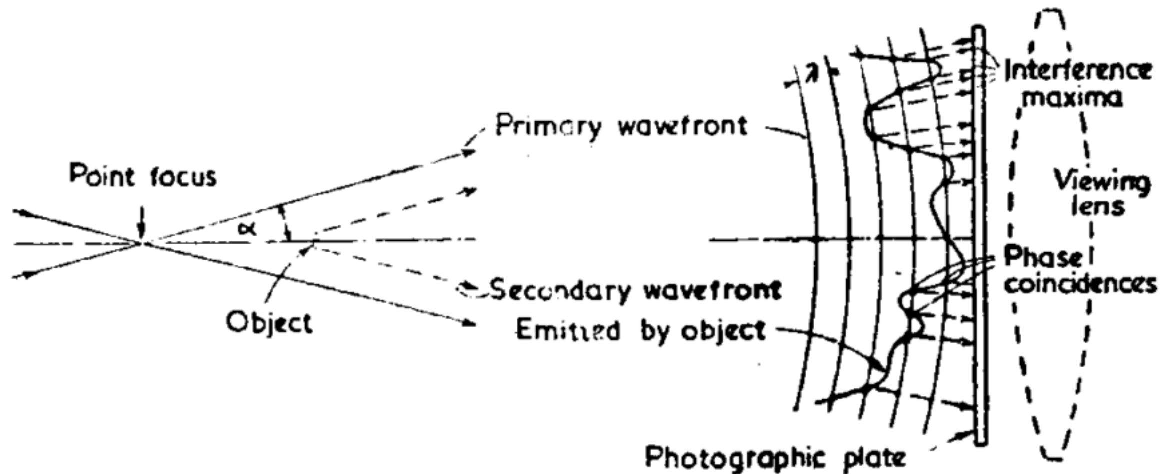

Figure 4.1: *Illustration taken from [1] illustrating Gabor's holographic principle. The incident electron beam is focused to a point before illuminating the object and the interference pattern created by the object wavefront and reference or primary wavefront.*

plitude and phase is exposed. In the Fourier transform of the hologram, there exist a set of bands containing the same phase and amplitude information, but with opposite sign. Due to the geometry of the setup the two bands are located on top of each other obscuring the information of the amplitude and phase. This is known as the twin image problem and is main problem of this technique as it distorts the information to be recovered.

4.2.1 Off-axis holography

In the wake of the struggle to solve the twin image problem, the Möllenstedt electrostatic biprism was invented [26]. The biprism is a thin wire located perpendicular to the optic axes, in one of the image planes of the microscope. Figure 4.2 shows how the object- and reference wave is overlapped by a positive bias on the biprism. The positive bias draws the electrons together and the overlap gives rise to an interference pattern containing both the phase and amplitude information. This describes the setup for off-axis holography.

The intensity for off-axis holography is described by equation (4.2) from the double slit experiment. And the geometry of the experimental setup solves the twin image problem by shifting the set of bands in Fourier space to opposite sides of each other. In this, it is possible to isolate and analyse only one. The information is then extracted by the inverse Fourier transform of the isolated band, resulting in a complex image. The phase ϕ and amplitude A may then be recovered by the following equations.

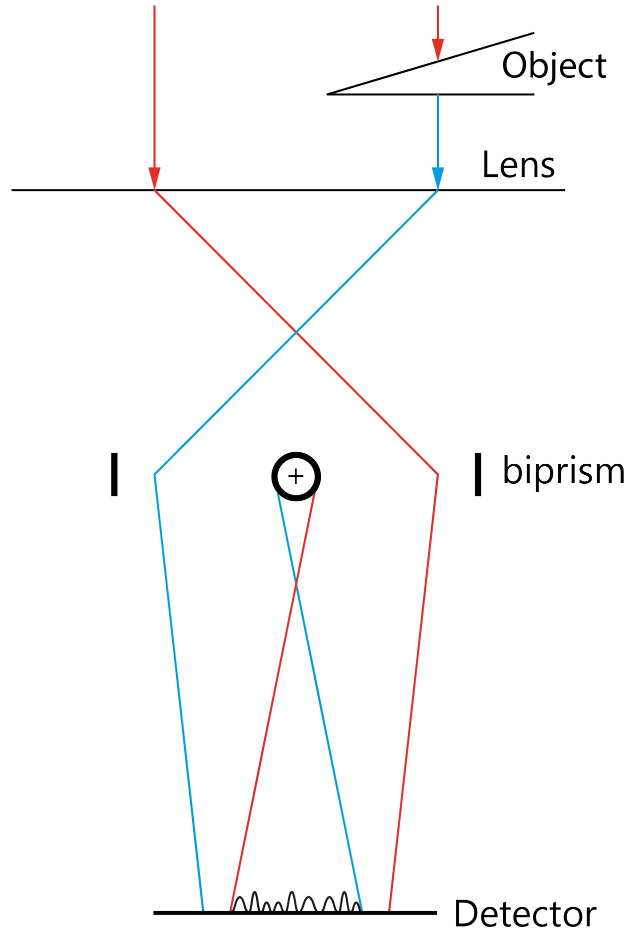

Figure 4.2: *Schematic setup of how the overlap between the object- and reference wave by the use of a Möllenstedt biprism is made in an off-axis holography experiment. The overlap created an interference pattern on the detector.*

$$\phi = \tan^{-1}\left(\frac{I_i}{I_r}\right), \tag{4.3}$$

$$A = \sqrt{I_r^2 + I_i^2}, \tag{4.4}$$

where I_r and I_i are the real and imaginary images, respectively, as stated by reference [25].

However, there are some limitations to off-axis holography. The most prominent is the need for a vacuum reference wave, which limits the area on the sample available for investigation. The microscope needs to be equipped with an electrostatic biprism, an expensive and highly specialized addition to a TEM.

4.2.2 Inline electron holography

Off-axis holography is one of several holographic methods [27–29]. With the invention of spherical aberration correctors (C_s-correctors) and the general increase in computing power, alternative methods for solving the phase problem have become available. Some of these methods are based on an image series taken while changing a known microscope dependant parameter affecting the electron wave, for example the defocus. From the image series, a reconstruction of the full wave function is obtained [2, 30, 31].

These techniques are independent of a reference wave and rely on interference of the object wave with itself. This complicates the reconstruction process in comparison with Off-axis methods, but it also removes the constraint of having a vacuum reference wave. In addition, the experimental setup only requires a TEM with an energy filter, which is a quite common feature that allows for other types of experiments in addition to holography.

Figure 4.3 illustrates how the different parts of the object wave interfere with each other. Large spatial frequency information (small distance information) is contained in small defocus steps and low spatial frequency information (large distance information) is contained in large defocus steps.

The general idea for reconstructing the full wave function, by changing the defocus, is as follows: An arbitrary object exit wavefunction is propagated to the back focal plane through the use of Fourier transform. In the back focal plane, a set of functions which are modelling the microscope are applied to the wavefunction. This creates a set of wavefunctions, one for different defocus values, corresponding to as set of experimentally acquired defocus images. The wavefunctions are then propagated to the image plane by Fourier transform. There they are subjected to a another set of functions that model the microscope detection process. A set of simulated images are then produced, each one corresponding to one of the experimental images. This is done by taking the intensity of each wavefunction separately. Each wavefunction is perturbed by the experimental image corresponding to the defocus of that wavefunction, before the wavefunctions are back propagated by Fourier transform to the back focal plane. In the back focal plane, the inverse of each microscope function is imposed onto each wavefunction, they are then back propagated to the object exit surface by another Fourier transform. There, a new wavefunction is created by the average of all defocused wavefunctions. Then the whole process repeats using the new wavefunction. This is done until either the desired number of iterations

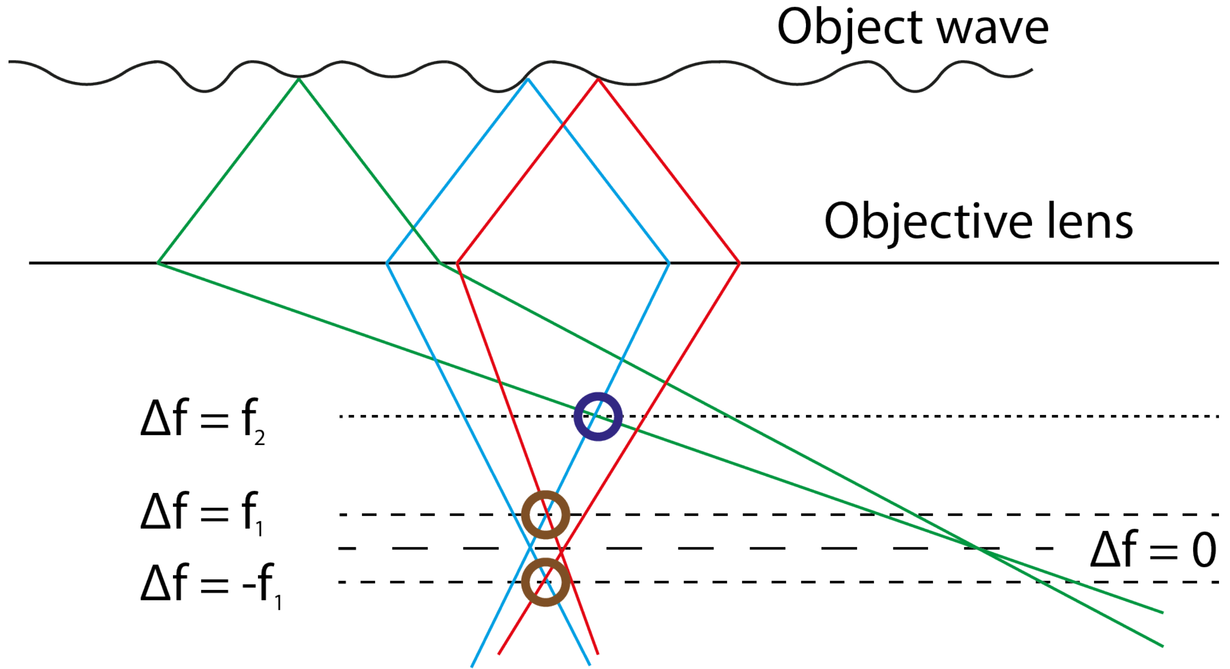

Figure 4.3: *Schematics of the principle of defocus series reconstruction. The different parts of the object wave interfere in the different focal planes. The brown circles on* $\pm f_1$ *illustrates that for small defocus parts of the object wave close to each other interfere. The blue circles illustrates that large defocus steps capture interference from parts of the object wave separated by large distances. This figure was inspired by [32].*

are performed or a convergence criteria is met. The output is the exit wavefunction.

A common assumption for these iterative approaches, is the phase object approximation (POA) [33, p. 486], where the object wave function i assumed to have the following form:

$$\Psi = e^{i\phi}. \tag{4.5}$$

This assumption is valid for thin objects, which is the case for TEM samples. The outcome of these iterative approaches is the exit wavefunction itself, the POA allows for a simple interpretation of the result where the intensity is given by equation (4.1). The phase may be retrieved as [34]

$$\phi = -i\ln(\Psi). \tag{4.6}$$

It is important to note that the phase found by these methods are not absolute, but relative with-

out any reference, thus, there is still a need for a vacuum reference for retrieving V_0. However, without a vacuum reference, the relative difference in potential may be obtained e.g. across an interface or grain boundary.

One problem with these iterative approaches is that they converge at a slow pace, despite the computation power of today's computers. This is due to the slow in recovery of the low spatial frequency information, which is discussed in more detail in following sections.

4.2.3 Transport of intensity equation

A different set of methods for solving the phase problem are the so-called deterministic approaches. These methods are built on the transport of intensity equation (TIE).

Under the paraxial approximation (small angle approximation) and for coherent waves, TIE was first derived by Michael Reed Teague [35]. Starting from the time independent wave equation in free space formulated as,

$$\left[\frac{\partial^2}{\partial z^2} + \bigtriangledown_\perp^2 + \left(\frac{2\pi}{\lambda}\right)^2\right]\Psi(\mathbf{r}_\perp) = 0, \tag{4.7}$$

Teague derived the TIE:

$$-\frac{2\pi}{\lambda}\frac{\partial I(\mathbf{r}_\perp, z)}{\partial z} = \bigtriangledown_\perp \cdot [I(\mathbf{r}_\perp, z) \bigtriangledown_\perp \phi(\mathbf{r}_\perp, z)]. \tag{4.8}$$

This relates the change in intensity, $I(\mathbf{r}_\perp, z)$, to the rate of change of the phase, $\phi(\mathbf{r}_\perp, z)$. Here, $\mathbf{r}_\perp = (x, y)$ is the in-plane postiton vector, and $\bigtriangledown_\perp$ is the gradient (Nabla) in the plane perpendicular to the propagation direction, z. The wave equation from (4.7) is the time independent Schrödinger equation in free space. Hence, the TIE is connected to the macroscopic and the microscopic wave phenomena. Also, TIE has been proven to have a unique solution for partially coherent waves as long as there are no zeroes in the intensity [36]. A complete derivation of TIE using the free space Schrödinger equation and with the same assumptions presented by Teague, is given by Barty et al. [37].

The intensity derivative, $\frac{\partial I(\mathbf{r}_\perp, \Delta f)}{\partial \Delta f}$, is usually approximated by using a finite difference method on images taken at different defocus Δf [38–41]. The images are usually taken at over and

under focus, enabling the retrieval of the phase correlated to an in focus image. Hence, a minimum of two images are needed to recover the phase of a third image. Figure 4.4 illustrates how the derivative relates a center image to images from planes on either side.

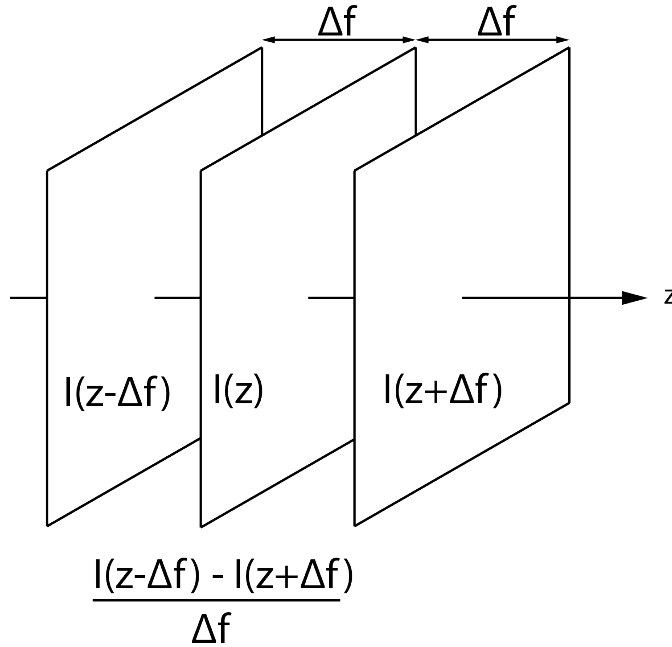

Figure 4.4: *The intensity derivative of TIE relate two adjacent intensity images to a central intensity image.*

Several methods for finding a solution for TIE have been devised. The earliest was presented by Teague [35], where he recasts the right hand side of eq. (4.8) as $\bigtriangledown_{\perp}\Psi = I(\mathbf{r}_{\perp}, z) \bigtriangledown_{\perp} \phi(\mathbf{r}_{\perp}, z)$ to achieve a Poisson equation, given as,

$$\bigtriangledown^2 \Phi(\mathbf{r}_{\perp}, \Delta f) = -\frac{2\pi}{\lambda} \frac{\partial I(\mathbf{r}_{\perp}, \Delta f)}{\partial \Delta f}. \tag{4.9}$$

This equation can be solved by the use of a Green's function solution.

An alternative approach would be through the use of Fourier transforms, where the gradient takes the form of a frequency vector by the Fourier transform as

$$\mathcal{F}[\bigtriangledown^2] = \mathcal{F}[\frac{\partial^2}{\partial x^2} + \frac{\partial^2}{\partial y^2}] = \mathcal{F}[\frac{\partial^2}{\partial x^2}] + \mathcal{F}[\frac{\partial^2}{\partial^2}] = -\frac{k_x^2}{4\pi^2} - \frac{k_y^2}{4\pi^2} = \frac{\mathbf{k}_{\perp}^2}{4\pi^2}, \tag{4.10}$$

this indicate that an inverse gradient may be written as [42]

$$\mathcal{F}[\bigtriangledown^{-2}] = \frac{4\pi^2}{\mathbf{k}_\perp^2}. \tag{4.11}$$

This indicates that the TIE will amplify low spatial frequency noise, strengthening long range real space errors. Fourier transforms impose periodic boundary conditions, which causes a problem as the boundary conditions for the phase are ill defined. In addition, defocusing usually causes distortions to the images, making the images in the image series different from each other. This is a problem as the numerical handling of the image stack assumes that one particular pixel in the images correspond to the same location in all images. If the image is rotated or magnified, this is no longer true and the calculation of the phase will be erroneous. However, TIE is still being explored as a method for solving the phase problem and to retrieve the mean inner potential, as well as recreate the wave function of a transmitted wave.

Chapter 5

Full Resolution Wave Reconstruction

In this section, we investigate the details of the Full Resolution Wave Reconstruction (FRWR) algorithm. Here, the different parts making up the algorithm will be presented, as well as a description of the process.

5.1 The Full Resolution Wave Reconstruction algorithm

Created by Christoph T. Koch, the Full Resolution Wave Reconstruction algorithm (FRWR) [2, 3] has successfully merged the two concepts of modern inline holography and TIE. Based on the Gerchberg-Saxton (G-S) algorithm [30], FRWR uses an iterative scheme to simulate a image series taken at different defocuses. This is done to reconstruct the electron exit wavefunction. By implementing a TIE like approach for recovering low spatial frequency information, and aligning the different images according to the simulated images, FRWR converge faster than similar algorithms [2].

The FRWR builds up a set of simulated images from the experimentally acquired images. These simulated images are then used in several processes of the algorithm, such as aligning the different images, updating the exit wave function and as a means to update the phase with a TIE like method. The simulated images are made from the following expressions [2, 3]

$$I_{\Delta}(\mathbf{r}_{\perp}) = |\mathcal{F}^{-1}[\mathcal{F}[\Psi_0(\mathbf{r}_{\perp})]CTF(\Delta f, \Delta\mathbf{k}_{\perp})E_{\Delta}(\Delta f, \Delta\mathbf{k}_{\perp})H(\Delta\mathbf{k}_{\perp})]|^2, \tag{5.1}$$

$$I(\mathbf{r}_\perp) = \mathcal{F}^{-1}\left[\mathcal{F}[I_\Delta(\mathbf{r}_\perp)]E_s(\Delta f, \Delta\mathbf{k}_\perp)MTF(\Delta\mathbf{k}_\perp)\right]. \tag{5.2}$$

Here, $I_\Delta(\mathbf{r}_\perp)$ is the intensity associated with events taking place in the back focal plane of the microscope. $I(\mathbf{r}_\perp)$ is the intensity simulated to coincide with the experimentally acquired images. $\Delta\mathbf{k}_\perp = (k_x, k_y)$ is the spatial frequency vector, $\mathbf{r}_\perp = (x, y)$ is the real space vector and Δf is the defocus. $\mathcal{F}$ and $\mathcal{F}^{-1}$ denotes the Fourier- and inverse Fourier transform, respectively.

In order to simulate the intensity, a description of the various *microscope functions* is needed. $\Psi_0(\mathbf{r}_\perp)$ is the object exit wave function (OWF) that contains the phase information of interest. The $CTF(\Delta f, \Delta\mathbf{k}_\perp)$, is the *coherent transfer function* (CTF) and is related to the *transmission cross coefficient* as described in more detailed by [3, 31, 43] and the objective lens of the TEM. It represent all distortions imposed on the OWF by the objective lens. The *defocus-spread-dependent envelope function* (DSE), $E_\Delta(\Delta f, \Delta\mathbf{k}_\perp)$, is related to the chromatic aberration, the fluctuations in high tension and lens current. $H(\Delta\mathbf{k}_\perp)$ is an aperture function that is unity for spatial frequencies below the range of frequencies $\mathbf{k}_{max}$. Following the flux preserving principle, explained by Koch in [3], the *partial spatial coherence envelope function* (PSE), $E_s(\Delta f, \Delta\mathbf{k}_\perp)$, is implemented as a convolution by the realspace intensity. The reciprocal interpretation of the point spread function of the detector is $MTF(\Delta\mathbf{k}_\perp)$, called the *modulation transfer function* (MTF). These functions are described in more detail below.

Expression (5.2) assumes that higher order aberrations, apart from those mentioned above may be neglected.

5.1.1 The coherent transfer function

As mentioned, the CTF describes the objective lens aberrations induced into the OWF. Common to all aberrations is that they may be modelled as a point spread functions that disturbs the signal being detected, limiting the resolution of the image. The CTF includes the effects caused by spherical aberration, defocus and astigmatism. The effect from all these are that they cause a spread of any point in the reciprocal space. It is defined as

$$\text{CTF}(\Delta\mathbf{k}_\perp, \Delta f) = e^{i\chi(\Delta\mathbf{k}_\perp, \Delta f)}, \tag{5.3}$$

where $\chi(\Delta\mathbf{k}_\perp, \Delta f)$ is the aberration function given as

$$\chi(\Delta\mathbf{k}_\perp, \Delta f) = \pi\lambda A\cos[2(\theta - \theta_A)]\Delta k^2 + C_s\frac{\pi\lambda^3\Delta k^4}{2} + \pi\lambda\Delta f\Delta k^2. \tag{5.4}$$

Here $|\Delta\mathbf{k}_\perp|^2 = \Delta k^2$ is the magnitude of the reciprocal vector in the plane perpendicular to the optic axis, $\theta_A = \tan^{-1}(k_y/k_x)$ is the angle related to the astigmatism of the objective lens, and C_s is the spherical aberration constant of the objective lens.

Astigmatism

The first term of equation (5.4),

$$\pi\lambda A\cos[2(\theta - \theta_A)]\Delta k^2,$$

represents the astigmatism. As the objective lens (OL) does not have perfect cylindrical symmetry, the electrons will be bent more strongly at certain regions in the lens than other regions. Figure 5.1 illustrates how an OL with a certain symmetry deflects the electrons differently at around the optical axis. Electrons entering the OL at the same radial distance from the optical axis will be deflected differently around the optical axis. The result is that the crossover point of the OL is spread out. The disc of least confusion is then the a disc where the spread is at a minimum.

The effect is best seen in the Fourier image of an amorphous material, taken at a slight defocus or away from the optimal (eucentric) height. Figure 5.2 shows a Fast Fourier transform (FFT) image taken of an amorphous region at a defocus. This illustrates how the isotropically scattered electrons become skewed by a astigmatic OL.

The amplitude A and the angle θ may be fully corrected for by stigmator coils in the TEM. Thus it is possible to remove this effect completely. Nonetheless, FRWR includes means to correct for astigmatism in the case it was not fully corrected for in the experiment.

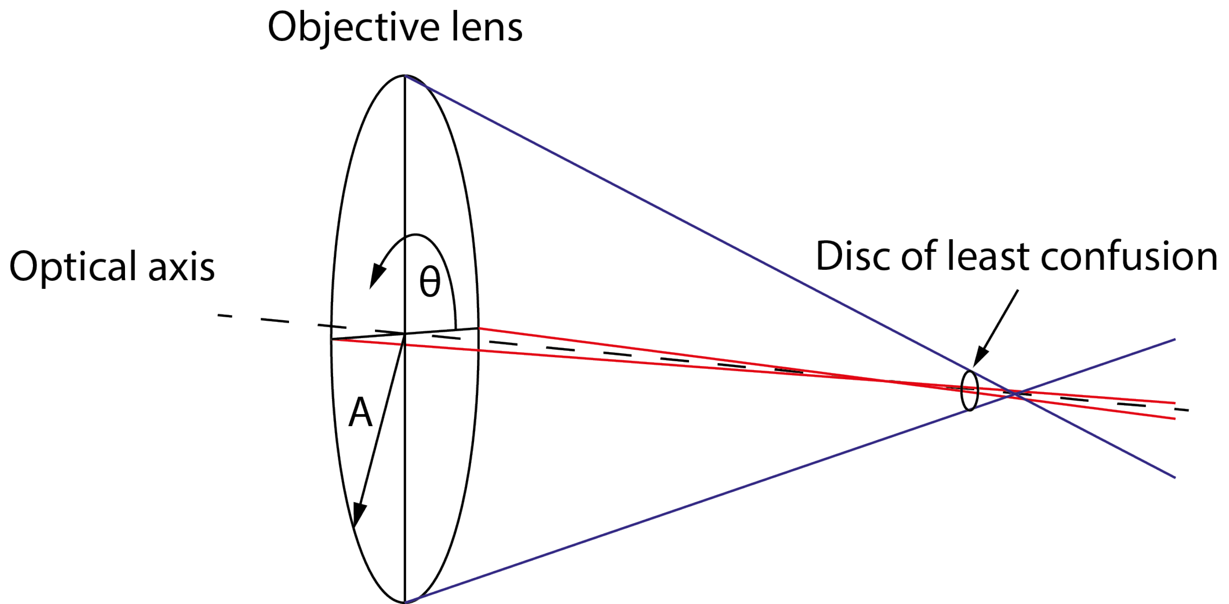

Figure 5.1: *As the electrons exit the objective lens, they will be bent according to the cylindrical symmetry of the lens. This causes a disc of least confusion in the reciprocal space.*

Spherical aberration

The second term of equation (5.4) is

$$C_s \frac{\pi \lambda^3 \Delta k^4}{2}.$$

Due to the non-uniform magnetic field of the OL, the magnetic Lorentz force interact more strongly with the electrons that are close to the edge of the lens than those close to the optical axis. The effect of this is that electrons entering the OL close to the optical axis converge at a point further away from the lens, while the electron entering the lens further away from the optical axis converge at a point closer to the lens. Figure 5.3 illustrates how electrons scattered from a single point on an object are collected by the OL and converges at different points according to where they entered the OL. This causes a focal spread in the image, reducing the resolution. This focal spread is described by a point spread function in realspace and in reciprocal space.

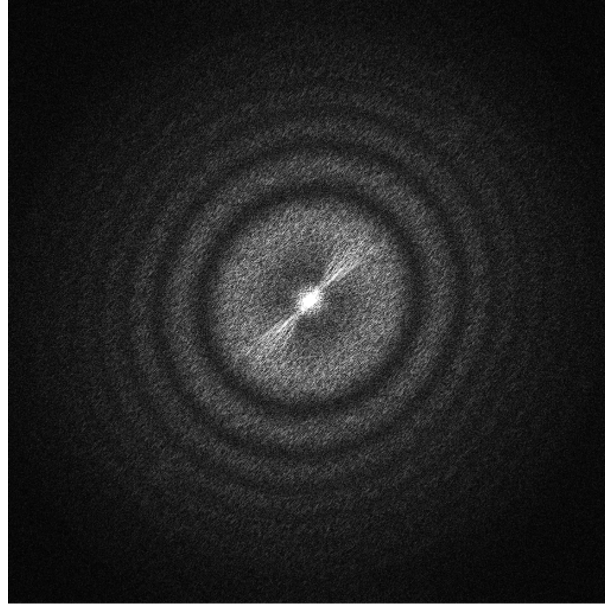

Figure 5.2: *Fast Fourier transform image taken of amorphous material at 960 nm defocus. The image shows the effect of astigmatism, causing imperfect circular symmetry of the Thon rings.*

Defocus

The defocus parameter is important. It is the aberration induced by the user, it is described by

$$\pi\lambda\Delta f\Delta k^2.$$

By inducing a change in the electric current of the OL the magnetic field affecting the electrons changes. By increasing the current, the strength of the field increases and the focal length of the OL decreases, this is over focus as the focus point lies above the in focus plane set by eucentric height. The opposite effect occurs if the lens current is decreased. In overfocus the electrons scattered by the object into the lens will be deflected more strongly, leading to a smearing of distinct features of the image. For images taken at either over- or underfocus, distinct features in the object appear at different positions. The effect may be described as "ghosts" from distinct features seeping out from its proper position in the image. This effect is discussed further later in section 6.3. The effect of defocus is illustrated in figure 5.4, where an electron beam entering the lens is deflected to a point closer to the lens by overfocusing the lens.

The CTF is understood as a bandpass filter for the spatial frequencies of the OWF. And the imaginary part of the CTF is the main contributor to filtering out spatial frequencies [2]. This is true under the weak phase object approximation where the OWF may be described as

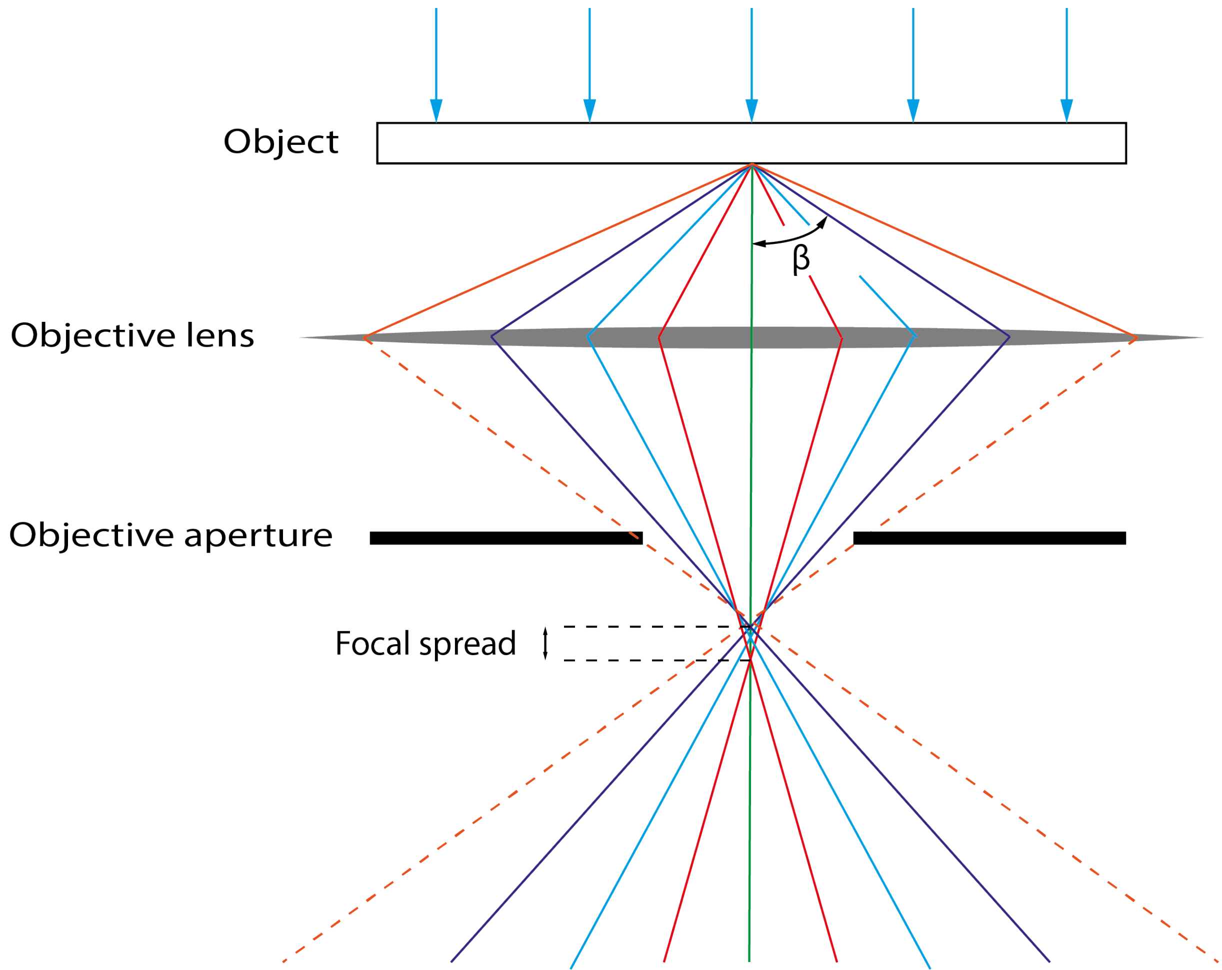

Figure 5.3: *Electrons scattered from a single point on the object gets collected at different points according to where they entered the objective lens. The electrons deflected closer to the optical axis will converge further from the lens.*

$$\Psi = 1 + i\phi. \tag{5.5}$$

Then, the only part contributing to the intensity is the imaginary part of the CTF. Scherzer found the optimal defocus value where the width of spatial frequencies captured are the largest called Scherzer defocus (Δf_{Sch}). By neglecting astigmatism, the scherzer defocus is given as [33, p. 485-494]

$$\Delta f_{Sch} = -1.2\sqrt{\lambda C_s}. \tag{5.6}$$

Figure 5.5 presents the shape of the imaginary part of the CTF for different defocus values.

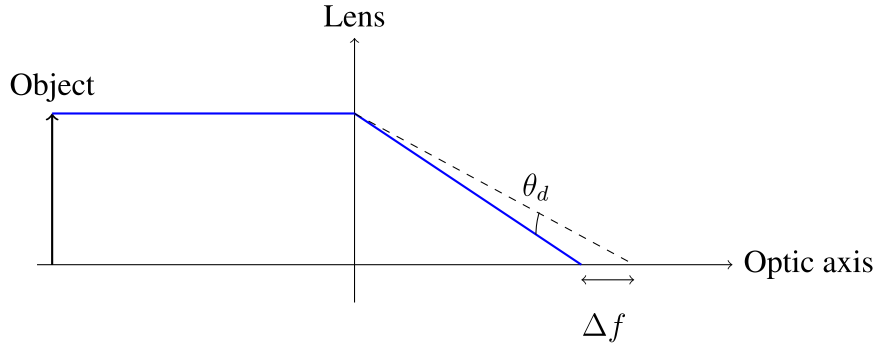

Figure 5.4: *Illustration of how the defocus change the path of an electron. The thick blue line illustrates the path taken with an overfocused lens, the dashed line illustrates a path that would be taken without a defocused lens.*

This illustrates how the CTF tends towards zero for the low spatial frequencies. In addition, some of the low spatial frequencies are recovered at higher defocus values, this confirms the statement from section 4.2.2; that low spatial frequencies are recovered by a large defocus and high spatial frequencies are recovered by small defocus.

To best capture a wide range of spatial frequencies the FRWR allows for the use of non-linear defocus steps. The defocus step (Δf_n) used when acquiring the different defocus images for an image stack are as follows [2]:

$$|\Delta f_n| = \Delta f|(n - n_{ref})^p| \tag{5.7}$$

n, n_{ref}, p and Δf are the number of images aquired, the number of the image sat at zero defocus, and the power to be used and the defocus step size, respectively. This allows for a broad range of defocus using less images which is needed to capture a wide range of spatial frequencies [44]. Most notably the Δf_n is the value used for the derivative in the TIE like approach used in FRWR.

5.1.2 The defocus-spread-dependent envelope function

With ever increasing performance of the TEM, the different instabilities of the microscope setup are decreasing. However, instabilities of the high tension and lens currents are not fully compensated for. The instabilities create a spread in in the exact focal point of the objective lens. This creates an envelope function in the reciprocal space

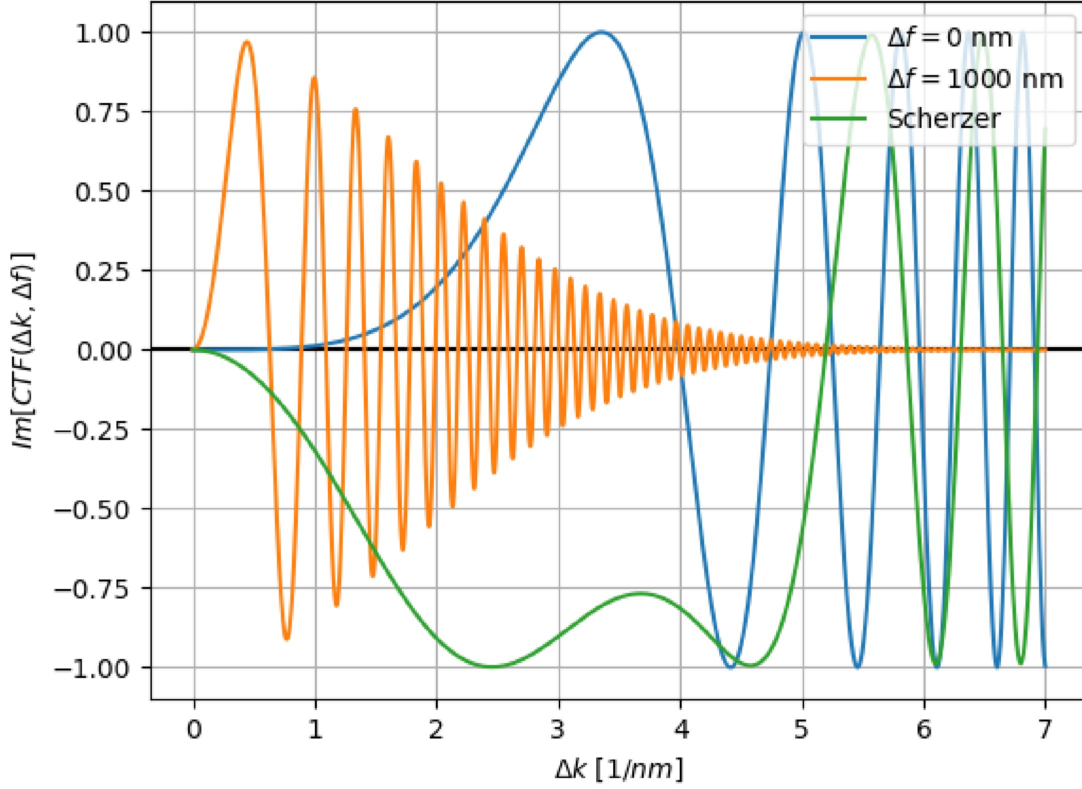

Figure 5.5: *The imaginary part of the coherent transfer function plotted for different defocus values. This plot is of a C_s = 0.5mm . A high tension of 200kV. The plot includes a direct multiplication by the partial spatial envelope function using α = 50 mrad. Astigmatism have been omitted in all functions.*

$$\Delta_f = C_c \sqrt{\left(\frac{\Delta E}{E}\right)^2 + 2\left(\frac{\Delta I}{I}\right)^2}, \tag{5.8}$$

$$E_\Delta(\Delta f, \Delta \mathbf{k}_\perp) = e^{-\left(\frac{(\pi \lambda \Delta_f k)^2}{2}\right)^2}. \tag{5.9}$$

Here, imperfections in the high tension ΔV and the lens current ΔI lead to a dampening of the higher spatial frequencies. C_c is the chromatic aberration constant of the microscope. Figure 5.5 illustrates how an envelope function works. However, the defocus-spread-dependent envelope affects the CTF less than illustrated by Figure 5.5.

5.1.3 Aperture function

The objective aperture is located in the back focal plane of the objective lens i.e. the reciprocal space. In the intensity for the simulated images of FRWR, it is defined as a cutoff function that is unity for all frequencies below a maximum frequency value $\mathbf{k}_{\text{max}}$,

$$H(\mathbf{k}) = \begin{cases} 1, & \lambda|\mathbf{k}| \leq \lambda\mathbf{k}_{\text{max}} \\ 0, & \lambda|\mathbf{k}| > \lambda\mathbf{k}_{\text{max}} \end{cases} \tag{5.10}$$

The cutoff frequency is defined by the user and should correspond to the size of the aperture used during an experiment. Measurements of the frequency reach of the objective aperture relevant for this thesis was carried out by the author, for the results from the measurements and further discussion on the objective apertures see appendix A.

It is important to note the correlation between Figure 5.5 and 5.2, where the first may be understood as a thin slice cut out form the latter. The Thon rings are the reciprocal representation of the intensity

$$I_{\Delta}(\mathbf{r}_{\perp}) = |\mathcal{F}^{-1}[\mathcal{F}[\Psi_0(\Delta f, \mathbf{r}_{\perp})]CTF(\Delta f, \Delta\mathbf{k}_{\perp})E_{\Delta}(\Delta f, \Delta\mathbf{k}_{\perp})H(\Delta\mathbf{k}_{\perp})]|^2.$$

This observation suggest that the the CTF is only an approximation as the absolute square of Figure 5.5 would not result in large areas where the spatial frequencies are zero. A more thorough explanation of how the CTF is found are given by Meyer el al. in [45].

5.1.4 Partial spatial coherence envelope

One of several ways FRWR is different from other wave reconstruction schemes is by its treatment of the partial spatial envelope function (PSE),

$$E_s(\Delta f, \Delta\mathbf{k}_{\perp}) = e^{-(\pi\alpha\Delta k^2[\Delta f + A\cos(2[\theta - \theta_A])])}, \tag{5.11}$$

where α is the semi convergence angle of the electron source. Conventionally the PSE was implemented as a multiplication of the PSE with the reciprocal OWF, the CTF and objective

aperture function. However, Figure 5.5 illustrates that a direct multiplication of the PSE leads to an envelope function that, not only dampen, but removes higher spatial frequencies for large defocus values. This indicates a loss of electron flux with defocus which is unphysical. To preserve the electron flux, the PSE is instead convoluted with the intensity created by the modulations to the OWF in the the reciprocal space, $I_{\Delta}(\mathbf{r}_{\perp})$, as stated by Koch in ref. [3].

5.1.5 The detector and its point spread function

One of the most wide spread methods for detecting TEM electrons is by a charge coupled device (CCD). A CCD is an array of photodetecting diodes or pixels. The top of the CCD is covered by a scintillator that converts electrons to photons for the photodetectors. Due to the scintillator having some finite height there will be some "leakage" of photons between neighbouring pixels, as illustrated in Figure 5.6. This "leakage" gives rise to a smearing of point objects in the image that may be described as a point spread function $\text{psf}_{sc}(\mathbf{r})$. The recorded image $I(\mathbf{r})$ will then be a convolution of the image formed by the microscope $I_m(\mathbf{r})$ and the point spread function.

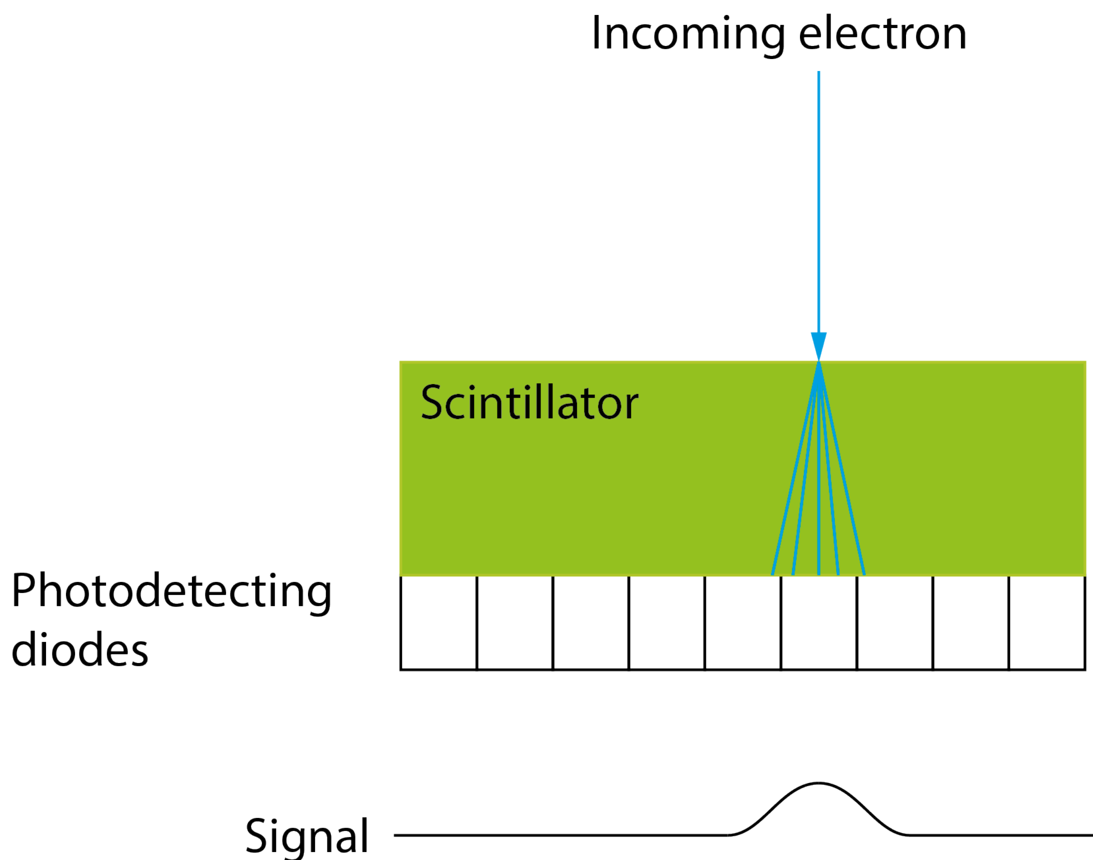

Figure 5.6: *The scintillator converts incoming electrons to photons that will scatter on to the photodetector underneath. However, the photons may hit neighbouring diodes resulting in a spread of the signal.*

The full impact that the CCD has on the image is decribed by

$$I(\mathbf{r}) \propto [I_m(\mathbf{r}) \otimes \mathrm{psf}_{sc}(\mathbf{r}) \otimes \mathrm{psf}_{px}(\mathbf{r})], \tag{5.12}$$

where $\otimes$ reprecent a convolution, $\cdot$ the scalar product and the $\mathrm{psf}_{px}(\mathbf{r})$ is the point spread function associated with each pixel of the photo detector, which dampens the intensity and causes aliasing problems for sampling of spatial frequencies above the Nyquist limit [46].

Modulation Transfer Function

The Fourier transform of the $psf_{sc}(\mathbf{r})$ term is called the Modulation transfer function $MTF(\nu)$. The $MTF(\nu)$ is a narrow peak in Fourier space that reduces the intensity of high spatial frequencies i.e. dampens the small details in the detected image.

Once the shape of the $MTF(\nu)$ is acquired, a curve fit using a gaussian and an exponential function will give the parameters needed as input to FRWR; The $MTF(\nu)$ is given below with A, B,C and D as fitting parameters used as input,

$$MTF(\nu) = Ae^{-B\nu} + Ce^{-D\nu^2}. \tag{5.13}$$

where ν is the frequency given as

$$\nu = \frac{1}{\Delta_{px}} \tag{5.14}$$

with Δ_{px} as the CCD pixels size.

With $\tilde{\Delta}_{px}$ as the physical pixel size, the correlation between the actual CCD pixel size, physical CCD pixel size, along with the magnification, MAG, is given by

$$\Delta_{px} = \frac{\tilde{\Delta}_{px} B}{MAG}. \tag{5.15}$$

B is the binning used.

One of the consequences of using a CCD for detection is that the images become digitalized. This means that each image is represented by a two dimensional array of the same size as the CCD and binning used.

5.2 Describtion of the FRWR algorithm

Through an iterative process involving a series of experimentally acquired images, a set of simulated images are created. A starting wave function $\Psi_0(\mathbf{r})$ is defined as the square root of the in-focus intensity, before applying equation (5.2), using the same defocus values as was used for the experimentally acquired images. This yields a set of images that simulate the experimental image series at their respective defocus planes. The wavefunction corresponding to each defocus plane is then updated, using a normalization that includes the experimental image from that defocus plane. The different images are then back propagated to the object exit plane of by applying a an inverse representation of each function that make up the intensity, as explained below.

The general layout of the FRWR algorithm are as follows:

1. Starting wave function amplitude are set according to the image of the defocus closest to zero and the starting phase is set to zero giving

$$\Psi_{j=0}(\mathbf{r}) = \sqrt{I_{\Delta f_n=0}(\mathbf{r})}. \tag{5.16}$$

2. $\Psi_j(\mathbf{r})$ is then propagated to the back focal plane (reciprocal space) via Fourier transform [47], where the CTF, DSE and objective aperture function is applied,

$$\Psi^{BFP}_{j,\Delta f_n}(\Delta\mathbf{k}) = \mathcal{F}[\Psi_j(\mathbf{r})]CTF(\Delta f_n, \Delta\mathbf{k})E_\Delta(\Delta\mathbf{k})H(\Delta\mathbf{k}). \tag{5.17}$$

3. The wavefunction is then propagated to the image plane

$$\Psi_{j,\Delta f_n}(\mathbf{r}) = \mathcal{F}[\Psi^{BFP}_{j,\Delta f_n}(\Delta\mathbf{k})]. \tag{5.18}$$

4. The intensity unaffected by the CCD is then given by

$$I_{j,\Delta f_n}(\mathbf{r}) = |\Psi_{j,\Delta f_n}(\mathbf{r})|^2 \tag{5.19}$$

5. To correctly preserve the electron flux [3], the intensity from the propagated wavefunction is then convoluted with PSE and MTF, according to equation (5.2). The convolutions are done in reciprocalspace according to the concolution theorem [48]. This produces the simulated images, given by

$$I^{sim}_{j,\Delta f_n}(\mathbf{r}) = \mathcal{F}^{-1}[\mathcal{F}[I_{j,\Delta f_n}(\mathbf{r})]E_s(\Delta f_n, \mathbf{k})MTF(\Delta \mathbf{k})]. \tag{5.20}$$

6. The wave functions at each focal plane are then updated by a small update $d\Psi_{j,\Delta f_n}(\mathbf{r})$, based on the difference between simulated images and experimental images $I^{exp}_{j,\Delta f_n}$

$$d\Psi_{j,\Delta f_n}(\mathbf{r}) = \sqrt{I^{exp}_{j,\Delta f_n}} - \sqrt{I^{sim}_{j,\Delta f_n}} \tag{5.21}$$

$$\Psi_{j+1,\Delta f_n}(\mathbf{r}) = \frac{[|\Psi_{j,\Delta f_n}(\mathbf{r})| + d\Psi_{j,\Delta f_n}(\mathbf{r})]\Psi_{j,\Delta f_n}(\mathbf{r})}{|\Psi_{j,\Delta f_n}(\mathbf{r})|} \tag{5.22}$$

7. The different wave functions are back propagated by multiplication of the corresponding inverted CTF by

$$\Psi_{j+1,\Delta f_n}(\mathbf{k}) = \frac{\mathcal{F}[\Psi_{j+1,\Delta f_n}(\mathbf{r})]}{CTF(\Delta f_n, \mathbf{k})} \tag{5.23}$$

8. All $\Psi_{j+1,\Delta f_n}(\mathbf{k})$ are then averaged, weighted by the envelope functions DSE and PSE. The weighting is done to exclude effects that the envelope functions have on the wavefunction, and is preformed as

$$w(\Delta f, \mathbf{k}) = E_s(\Delta f, \mathbf{k})E_{\Delta_f}(\mathbf{k}) \tag{5.24}$$

$$\Psi^{avg}_{j+1}(\mathbf{k}) = \frac{\sum_{\Delta f} \Psi'_{j+1,\Delta f}(\mathbf{k})w(\Delta f, \mathbf{k})}{\sum_{\Delta f} w(\Delta f, \mathbf{k})} \tag{5.25}$$

9. The aperture function $H'(\mathbf{k})$ affecting $\Psi^{avg}_{j+1}(\mathbf{k})$ is imposed by a smooth exponential, as a hard cut off to the spatial frequencies by k_{max} may introduce artefacts. The power term q

must be chosen depending on the level of noise. Larger values for less noise [34]

$$A = \frac{1}{k_{max}} \sqrt[q]{-ln\left(\frac{1}{N}\sum_{\Delta f} w(\Delta f, k_{max})\right)} \tag{5.26}$$

$$H'(\mathbf{k}) = e^{(-(A|\mathbf{k}|)^q)} \tag{5.27}$$

$$\Psi_{j+1}(\mathbf{k}) = \Psi^{avg}_{j+1}(\mathbf{k})H'(\mathbf{k}) \tag{5.28}$$

10. Then the exit wave function is back propagated to the sample exit surface and the process repeats from step 2.

$$\Psi_{j+1}(\mathbf{r}) = \mathcal{F}^{-1}[\Psi_{j+1}(\mathbf{k})] \tag{5.29}$$

$$\Psi_j(\mathbf{r}) = \Psi_{j+1}(\mathbf{r}) \tag{5.30}$$

This is done until the number of iterations sat by the user is reached.

5.2.1 Image alignment

One of the most important aspects of any reconstruction algorithm it that the different defocused images needs to be spatially correlated to each other. As mentioned the images are digitized and computationally represented as two dimensional arrays. FRWR algorithm assumes that element (x,y) from an image taken at defocus step A will correspond to the same element (x,y) from an image taken at a different defocus B. If the image taken at defocus A is shifted, then the element (x,y) of image A and B will not correspond to the same point of the object. Figure 5.7 illustrates how a element, marked by purple in the different arrays is assumed to correlate with each other. If the different elements do not correlate to each other, then the reconstruction of the wave function will be faulty.

Therefore, a good image alignment method is needed. The image alignment in FRWR is done by minimizing a relative shift vector $(\Delta x, \Delta y)$. This is done using the experimental image and its simulated image given by [3]

$$\xi(\Delta x, \Delta y)^2 = \sum_{x=x_{left}}^{x_{right}} \sum_{y=y_{left}}^{y_{right}} [I_{exp}(x+\Delta x, y+\Delta y) - I_{sim}(x - x_{left}, y - y_{left})]^2. \tag{5.31}$$

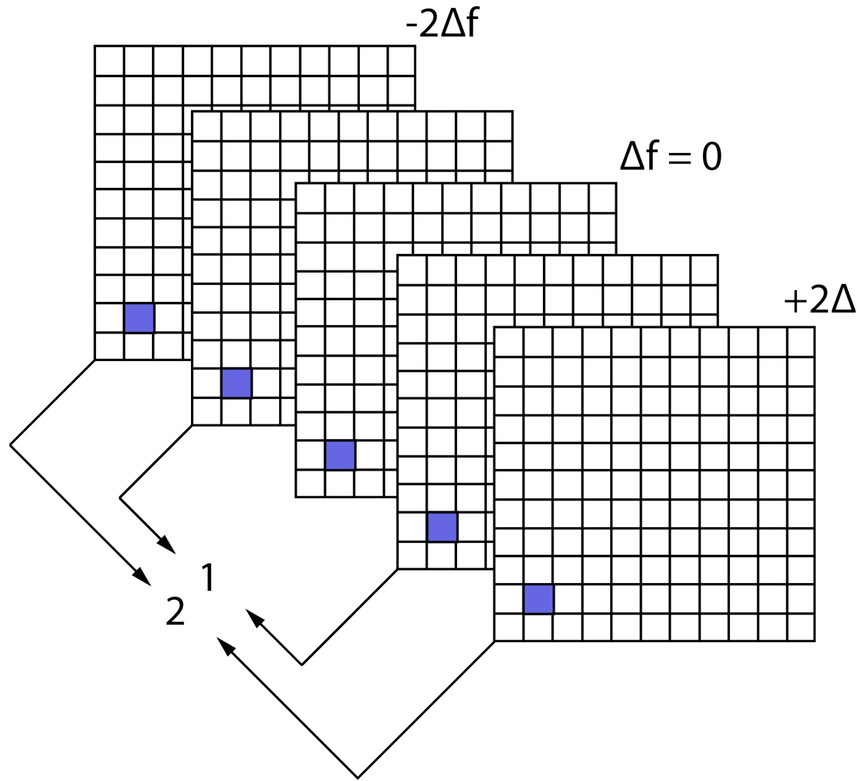

Figure 5.7: *The purple pixel in each image (illustrated by the five grids) represent an array element which should correspond to the same point for each image. The images on each side of the center image (Δf = 0) are incorporated during the alignment process before moving on the the next set of images.*

Here, the use of a sub region from an image is made possible. $(x_{right}-x_{left}, y_{right}-y_{left})$ defines the sub region. The images are incorporated sequentially, starting with the images closest to the minimum defocused image, the center image. This is done iteratively in accordance to the FRWR steps explained above, excluding step 6. As illustrated in Figure 5.7, the images are included symmetrically about either side of the center image. First the image with the smallest relative shift vector is included and aligned, then the image on the other side of the center image is included and aligned. After each image pair is aligned, the FRWR algorithm runs a user defined number of iterations. Then the next set of images are included and aligned in the same manner.

In addition to compensating for image shift, FRWR also compensates for other distortions such as rotation, magnification, barrel and pincus, as discussed by Koch in ref. [2].

5.2.2 Transport of intensity equation in FRWR

During the general algorithm presented in section 5.2, a unique version of the transport of intensity equaton, mentioned in section 4.2.3, has been implemented into the FRWR algorithm by Koch [2, 3]. This results in higher rates of convergence for FRWR, compared to similar algorithms. The major difference between the conventional TIE and the one used by FRWR is that the intensity derivative is approximated by the difference between the experimental and simulated image divided by the defocus of the two images:

$$\frac{I_{exp}(\mathbf{r}, \Delta f_n) - I_{sim}(\mathbf{r}, \Delta f_n)}{\Delta f_n} \Leftarrow \frac{\partial I(\mathbf{r}, \Delta f)}{\partial \Delta f}. \tag{5.32}$$

By then solving the TIE using Fourier transforms, a phase is calculated for each defocus. These phases are then added together as a weighted sum creating a phase update. This phase update is then added to the phase of the exit wave function in step 10 of the general algorithm mentioned above. However, it is important to note that the phase update is only added to the wavefunction if it is below a user defined threshold, normally around 0.1 rad. The phase update is calculated accordingly,

$$\phi_{upd}(\Delta\mathbf{k}) = \frac{\sum_{\Delta f_n} w(\Delta\mathbf{k}, \Delta f_n)\phi(\Delta\mathbf{k}, \Delta f_n)}{\sum_{\Delta f_n} w(\Delta\mathbf{k}, \Delta f_n)}, \tag{5.33}$$

where

$$w(\Delta\mathbf{k}, \Delta f_n) = \frac{e^{-(\Delta\mathbf{k}/k_{FH})^2}[1 - e^{-(\Delta\mathbf{k}/k_{FL})^2}]}{-4\pi^2\Delta\mathbf{k}^2}, \tag{5.34}$$

$$k_{FL} = \sqrt{\frac{CTF_L}{\pi\lambda|\Delta f|}}, \tag{5.35}$$

and

$$k_{FH} = \sqrt{\frac{CTF_P}{\pi\lambda|\Delta f|}}. \tag{5.36}$$

Here $\phi_{upd}(\mathbf{k})$ is the phase update. The weighing function $w(\Delta\mathbf{k}, \Delta f_n)$ operates as a pass filter

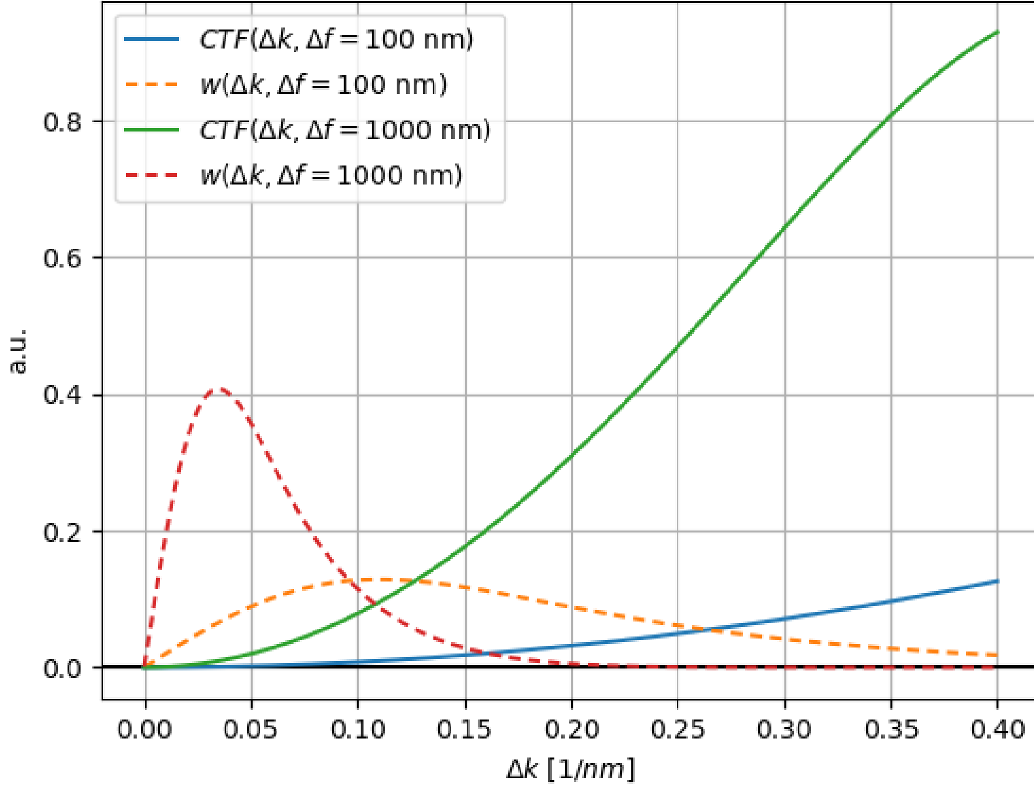

Figure 5.8: *The weighting function described by equation* (5.34), *for the different phases (dashed lines) limits the range of spatial frequencies according to the CTF (solid line). This was made using defocus values of 100 nm and 1000 nm, at a high tension of 200kV. The CTF was plotted by equation* (5.3) *excluding astigmatism.*

for each phase contribution, such that the phase updates for large defocus images contribute with low spatial frequency information and the phase updates for images taken at a small defocus steps contributes with high spatial frequency information. The CTF_L is the noise level defined normally as 0.02 reducing the high spatial frequencies to be included by the phases. CTF_P is set as 3. This corresponds to the region where the CTF stops acting linearly.

The FRWR version of the TIE acts as a bandpass filter, by only allowing for spatial frequencies, where the CTF is assumed to be linear. Other conventional algorithms work well for the recovery of high spatial frequencies but poorly for low spatial frequencies. The implementation of TIE helps recover the low spatial frequencies. This increase the rate of convergence for FRWR compared to other algorithms as stated by Koch in reference [2].

5.2.3 Gradient flipping of the phase

In addition the FRWR has implemented a feature called gradient flipping (GF) that acts on the phase of the electron wave. The purpouse of GF is to accentuate jumps in phase by dampening small variations, that may arise due to noise. GF work on the gradient of the phase. By identifying parts of the gradient of the phase that has a magnitude below a user-defined threshold. Then, those parts of the gradient is multiplied by a negative number lower than one i.e. flipping the phase. The flipped and un-flipped gradients are added together making the gradient lower and hence the phase in that region smoother. For more details see references [49–51]. GF works as a supplement for TIE as TIE tends to amplify low spatial frequency noise, while GF reduces this noise.

Chapter 6

Experimental results and discussion

In this chapter experimental results will be presented. First a brief presentation of the general experimental setup and method will be given. Then, we investigate the importance of the objective aperture in avoiding experimental artefacts, before measurements of the mean inner potential for Cu_2O are presented. Here we also investigate the effect that energy filtering has on the electron phase. Finally, results from measurements of the potential of a Cu_2O/CuO/ZnO heterostructure are presented and discussed.

6.1 Experimental details

Acquisition of the experimental data was done by the use of two different TEM instruments. The first one is the JEOL2200FS located at the Humboldt University, Berlin. The other is the JEOL2100F, located at the Department of Physics, University of Oslo. Both are equipped with a ZnO/W(000) Shottky FEG operated at 200kV high tension, and have an Ultra high resolution pole piece with C_s of 0,5 mm and C_c of 1,1 mm. The main differences are the cameras and energy filters. The JEOL2200FS is equipped with a MultiScan CCD Camera 794 Kodak camera and an in column omega-filter, while the JEOL2100F has a Gatan imaging filter (GIF) equipped with an US1000 FTXP camera. A more detailed discussion of the energy filters is found in Appendix C.

6.1.1 Experimental setup

To attain a focal series a well aligned TEM is important. This is important as defocusing will cause the projected image to change. These changes are primarily rotation, shift and magni-

fication. A well aligned microscope reduces these distortions. To simplify the experimental procedure, a Digital Micrograph (DM) plugin named FRWRtools has been created by Koch [52]. This plugin contains several tools that help with the acquisition and post processing of the results. The most important tools found in FRWRtools are:

- Acquire focal series, allows for the automated acquisition of a focal series by the TEM instrument.
- Auto align, will roughly align the different images of the stack.
- FRWR setup, creates a .cdf (common data format) file that is needed for the reconstruction process. This is discussed in further detail in a following section.
- Read image, enables DM to read and present a .img file.
- Create image stack, will enable the collection of several .img files to be put together into a .dm3 image stack that can be processed by DM. This is useful as the FRWR reconstruction software produces the set of simulated images as separate files along with separate files of the aligned experimentally aquired images.
- Show comparison, enables a direct comparison of two .dm3 image stacks. It is used to show the difference between simulated and experimental images located in the same position of two image stacks. This is done to check the validity of the reconstruction.

FRWRtools has several other features not mentioned here, however, these mentioned are the ones used most frequently.

6.1.2 FRWRsetup tool

To convert a defocus image stack from .dm3 to .cdf, the FRWRsetup tool must be applied. During this process the user sets parameters such as the spherical aberration, astigmatism, size of objective aperture and astigmatism. Further details can be found in references [2] and [52].

6.1.3 FRWR reconstructions

After the .cdf file has been produced the reconstruction procedure described in chapter 5 may begin. This is done by a separate software titled FRWR3. The software takes two input files, the .cdf file and a configuration file, that contains the specific settings to be used during the

reconstruction. The configuration file includes the number of iterations to be used and padding settings among other features. The output of a reconstruction is a phase image and an amplitude image.

6.2 Samples used in this thesis

The samples studied in this thesis was all provided by S. Gorantla and were part of a recent study reported by Gunnæs et al. [53] , Gan et al. [54] and Jensen et al. [55]. The goal of the study was to create a multilayer photovoltaic cell consisting of a Cu_2O/ZnO transparent layer for harvesting parts of the solar spectrum that a conventional Si cell could not absorb. Unfortunately, the structure favours the creation of a roughly 5 nm CuO intermediate layer, which makes up the Cu_2O/CuO/ZnO heterojunction studied in this thesis. Figure 6.1 presents the differnt layers of the structure.

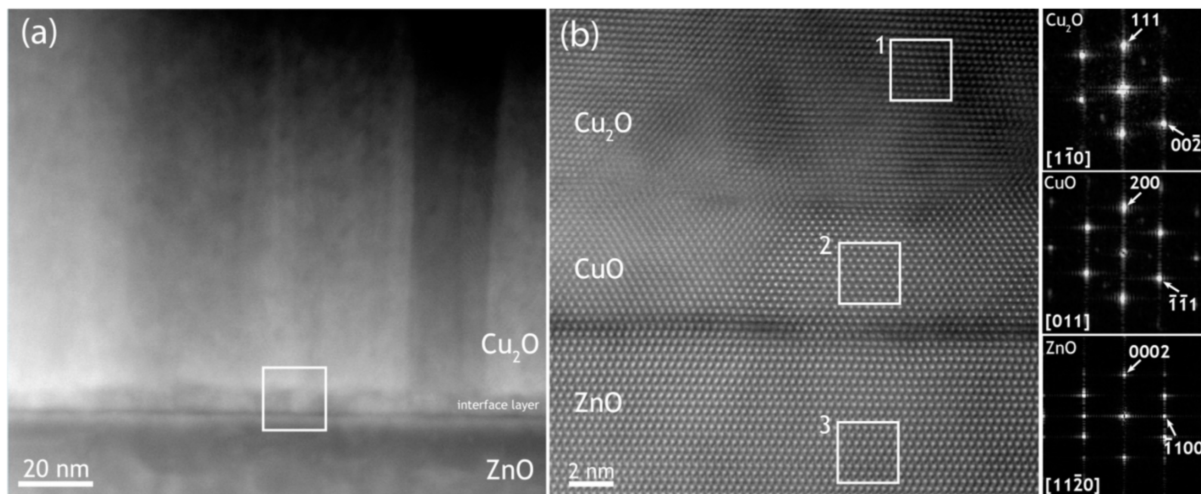

Figure 6.1: *(a) and (b) presents scanning TEM HAADF images of the Cu_2O/CuO/ZnO layers indicating the interface layer of CuO. Furthermore, the selected area diffraction images are given of the different regions to the right. Figure taken from Gunnæs et al. [53].*

During the same project, a TEM sample consisting of Cu_2O grown on a glass substrate was produced. This sample is used to study the mean inner potential of Cu_2O in this thesis.

6.3 Investigation of the importance of the objective aperture

To investigate the effect of the objective aperture, two focal series with and without objective aperture was captured. The results presented in Figure 6.2 show the effect of not having an objective aperture inserted. Figure 6.3 displays the same area imaged using an objective aperture.

The effect may be described as "ghosts" of distinct features moving out from the image and in to the region of vacuum, at large defocus.
By viewing the electrons in terms of classical optics as illustrated in Figure 6.4, rays coming from any point on the object will meet at two separate points in the image. One of the roles of the objective aperture is limit the rays by preferably isolating the (000) diffraction spot.

To investigate the effect from "ghosts" on the output of the FRWR algorithm, a reconstruction of the image stack used in Figure 6.2 was conducted. The resulting phase image is presented in Figure 6.5.
This illustrates that the FRWR algorithm does not handle the "ghost" effect in a proper manner. Any experiment should therefore be done by applying an objective aperture to eliminate the effect of "ghosts". As the effect is most prominent at large defocus, it would be tempting to reduce the defocus range as to dampen the effect. However, this is not a useful situation, as it would make the recovery of the small spatial frequencies difficult. A possible disadvantage of using a small objective aperture is that is limits the high spatial frequencies, and for a focus series taken at medium to low magnifications, about 80 kx magnification or lower, the smallest objective aperture (5 μm) will severely limit the resolution.

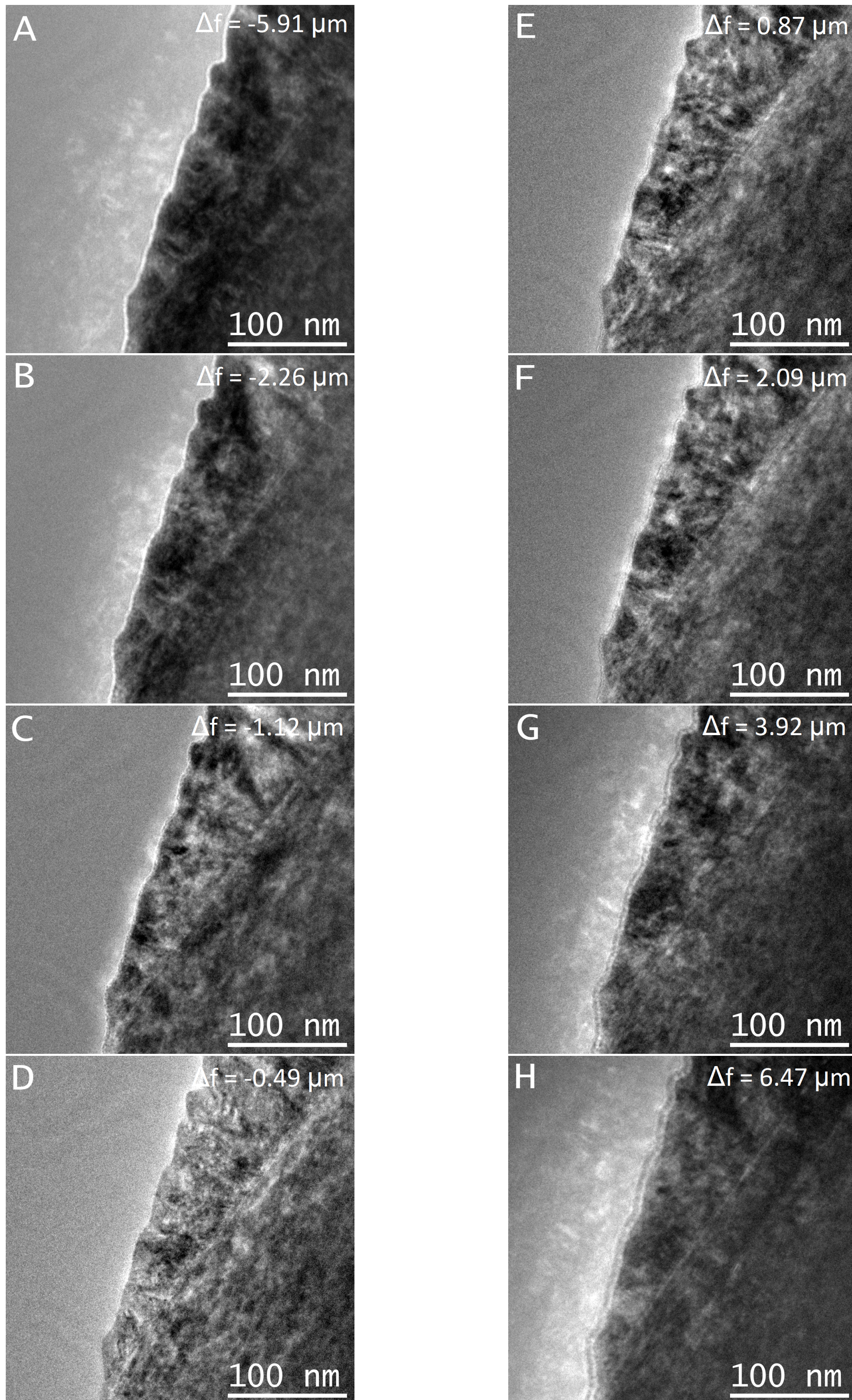

Figure 6.2: *Images showing the consequence of not using an objective aperture and making a focal series. The top left figure is taken at -5.91 μm defocus and following down the column for lower defocus ending at the bottom right figure taken at 6.47 μm defocus. Note the ghost like features coming out from the object edge.*

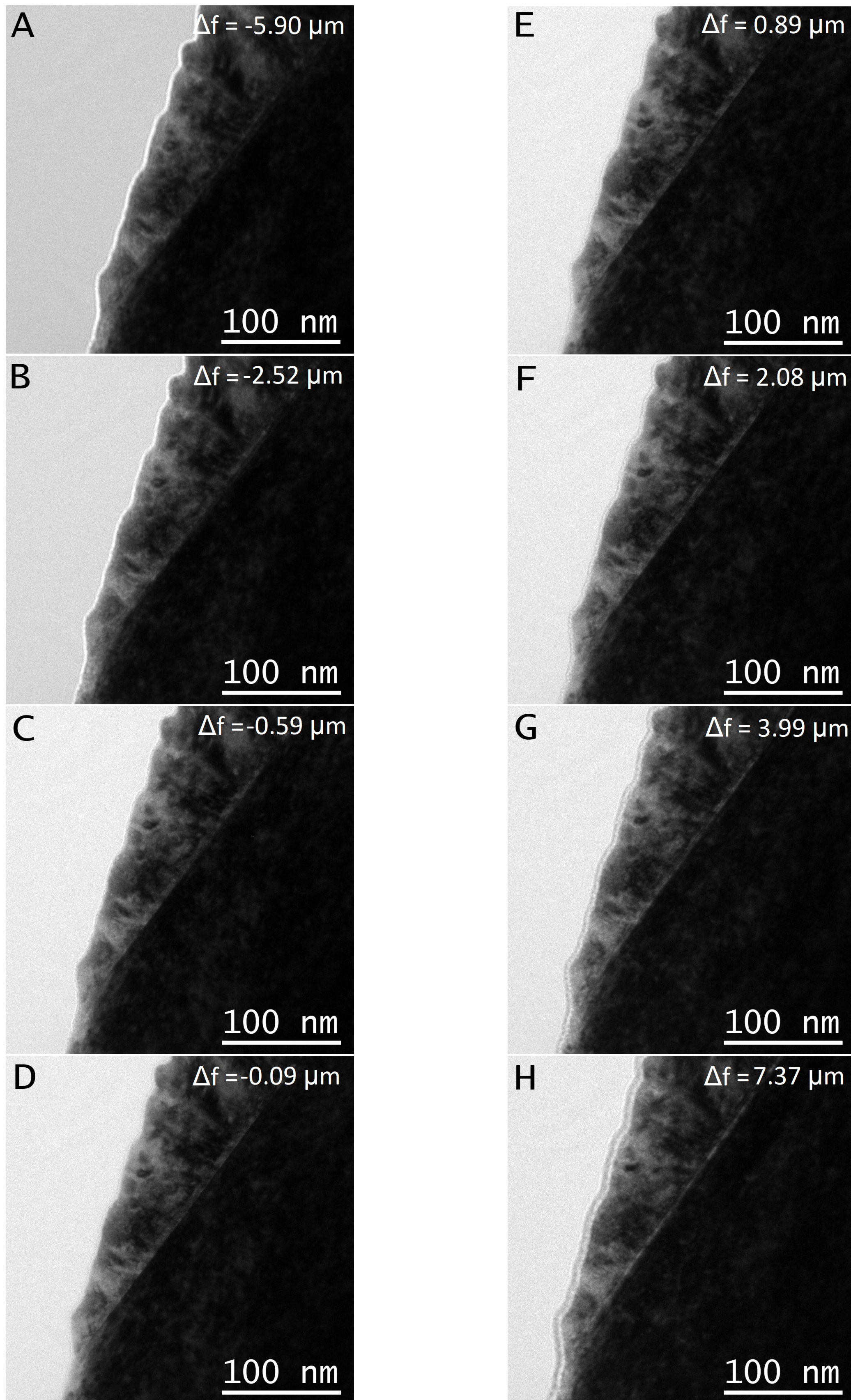

Figure 6.3: *Images taken with a 20 μm objective aperture covering the (000) reflection. Images are taken from same area as shown in Figure 6.2 to illustrate the effect of using an objective aperture versus not using one. The top left figure is taken at -5.9μm defocus and following down the column ending at the bottom right figure is taken at 7.37μm defocus.*

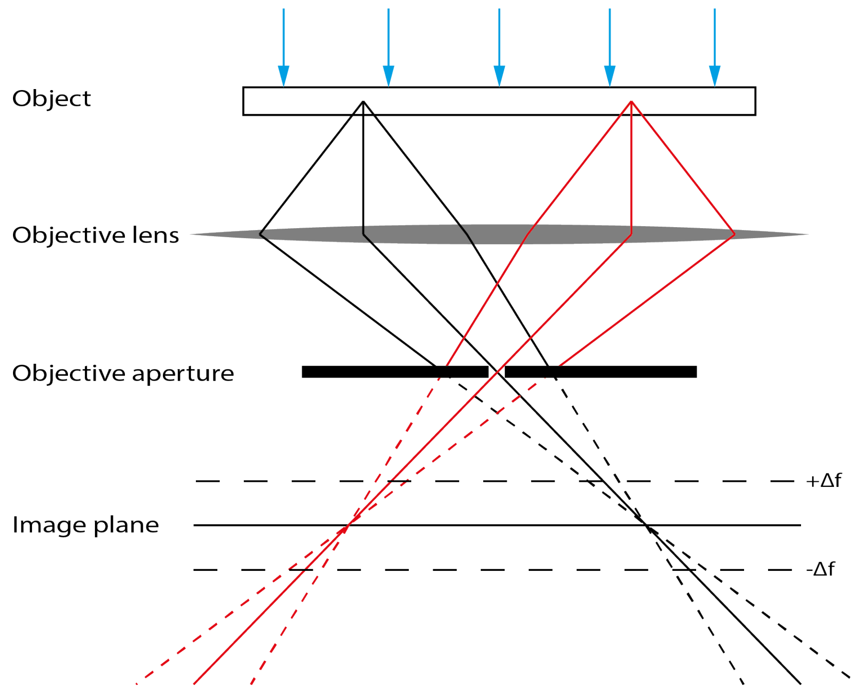

Figure 6.4: *Illustration of how the electron rays meet in two different points in the defocused image plane. The objective aperture will eliminate the ghost like features of the defocused image.*

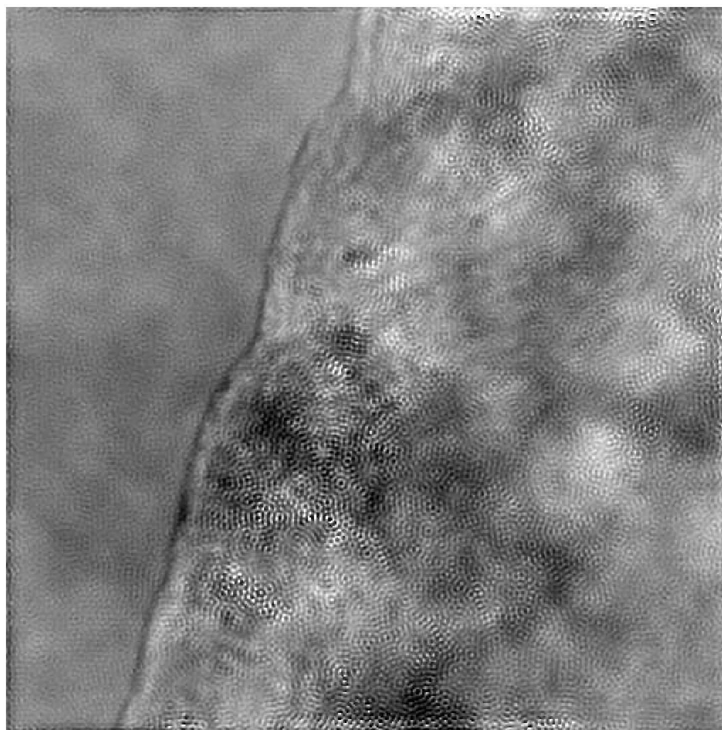

Figure 6.5: *Image of failed reconstructed electron phase. The phase was made from a section of the image stack presented in Figure 6.2.*

6.4 Effect of energy filtering in the mean inner potential measurements of Cu_2O

An investigation of the mean inner potential of Cu_2O grown on a glass substrate was conducted. The most promising site was close to the substrate-Cu_2O interface and a Cu_2O grain boundary shown in Figure 6.6. In particular the site was electron transparent and had no signs of bending or other artefacts.

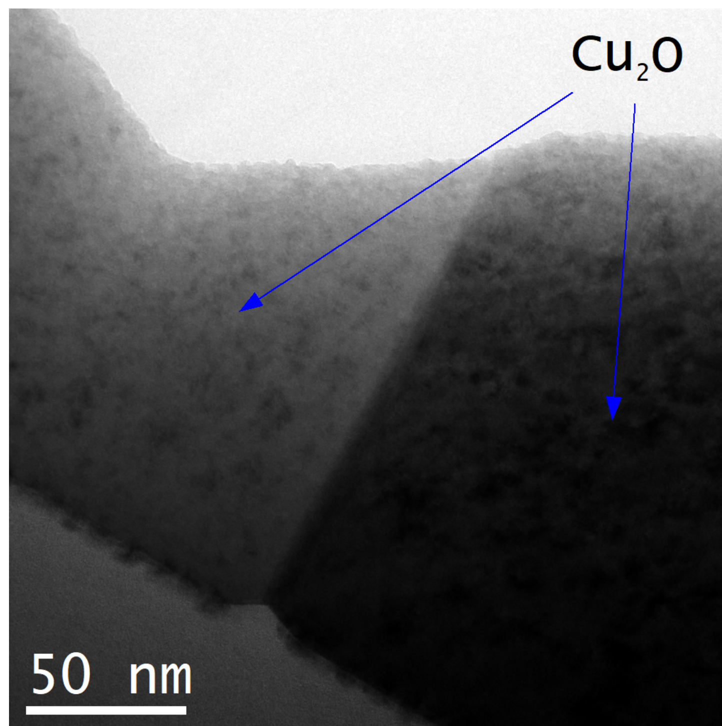

Figure 6.6: *Overview figure of two differently oriented Cu_2O grains grown on a glass substrate. The substrate is visible in the lower left of the figure.*

To explore the effect of energy filtering on the mean inner potential, two separate defocus series was acquired. The sample was tilted out of zone axis and an objective aperture of 20 μm was applied, thereby isolating the central reflection. The first defocus series was obtained using a energy filter of 10 eV slit width, centred around the zero loss region. The second was acquired after removing the energy slit. Both series consists of 31 images spanning the defocus range from -3.8 μm to +3.2 μm, taken with quadratic defocus increments. The magnification used was 80 kx and each image had a 2 sec. acquisition time. Figure 6.7 shows the reconstructed phase images from the two focal series.

After recording the last focal series, the objective aperture was removed. Then, two images of

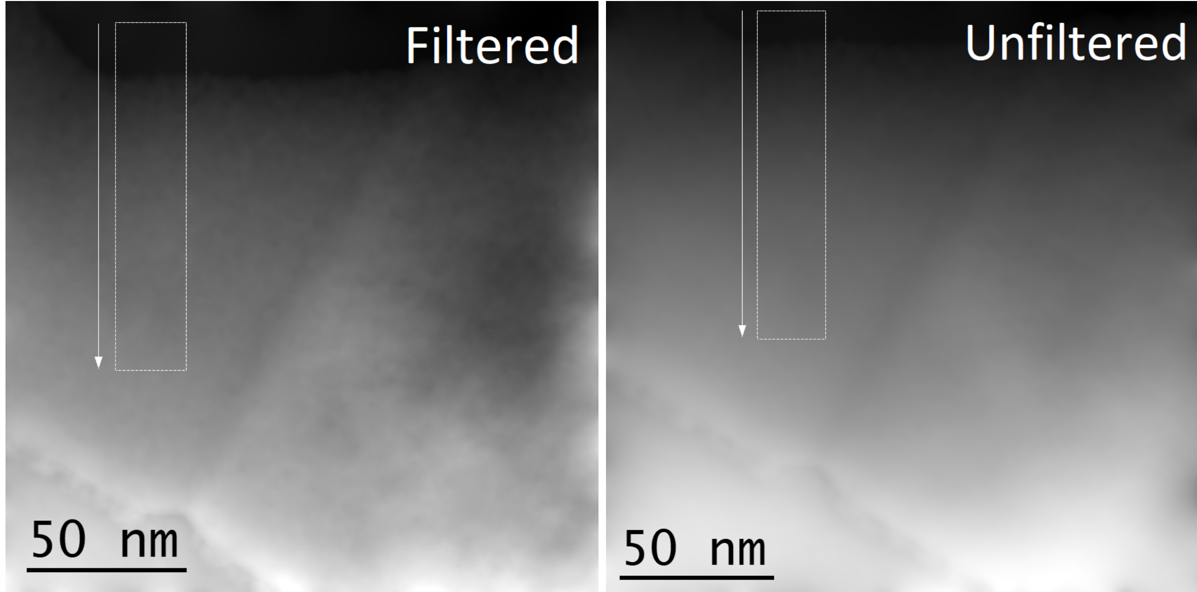

Figure 6.7: *Phase images produced by the FRWR algorithm. The image to the left stems from the energy filtered defocus series. The image to the right was made from the unfiltered defocus series. Both images contain a 100 pixels wide region used to make the profiles shown in Figures 6.8, 6.9 and 6.10.*

the same region as shown in Figure 6.6 were recorded in order to estimate the thickness. One image was acquired applying an energy slit width of 10 eV, resulting in an image (I_0) containing only electrons that had lost close to zero energy lost (elastic image). The other image (I_t) was made without any energy filter (inelastic image). An estimate for the thickness, t_{img}, of the sample was made by applying the log ratio method [56, p.249] to the two images, given by

$$t_{img} = \lambda_i \ln \left(\frac{I_t}{I_0} \right) . \tag{6.1}$$

Here, λ_i is the material dependent inelastic electron mean free path, and the log ratio method is discussed in more detail in Appendix D. By applying the log ratio method to the elastic- and inelastic images, an image given in units of mean free path (m.f.p.) was obtained. The inelastic mean free path of Cu_2O was calculated to 71.62 nm as explained in Appendix D. Figures 6.8 and 6.9 show two phase profiles and two thickness profiles, respectively. Each profile is extracted form an average across the 100 pixel wide regions presented in Figure 6.7. In both Figures the top profiles are from the energy filtered defocus series and the bottom profiles are from the unfiltered defocus series.

Images containing the potential was extracted from the relation given in equation (3.15), for-

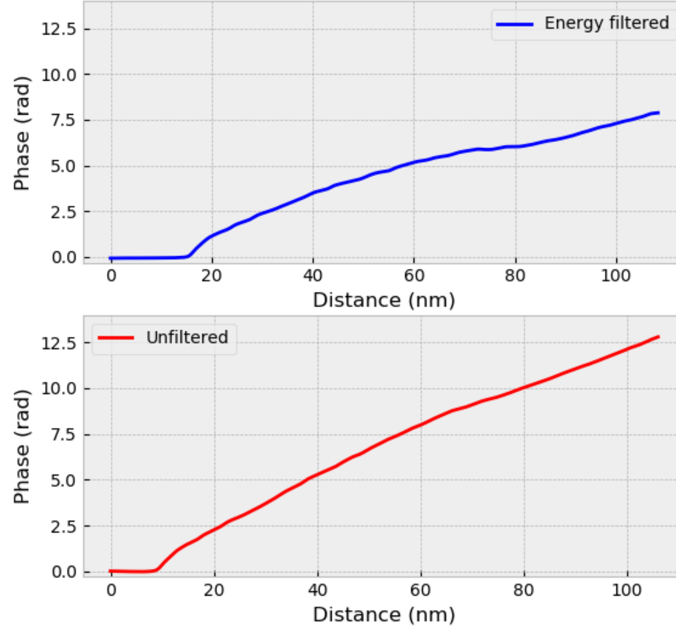

Figure 6.8: *Phase profiles of Cu_2O. The figures are made along the direction pointed out by the arrow in the images given in Figure 6.7. The top profile was made by the average value of the width (100 pixels) of the regions outlined in the left image of the mentioned figure. The bottom profile was done in the same manner from the region outlined in the right image, also, from the mentioned figure.*

mulated here as

$$V_0 = \frac{\Delta\phi_i}{C_E t_i}. \tag{6.2}$$

As the two phase images have a different field of view of the sample, two subregions of the thickness image had to be extracted according to each of the phase images. By multiplying the thickness sub regions (t_i) by the interaction constant given as C_E = 0.007288 rad(Vnm)$^{-1}$ an image corresponding to $C_E t_i$ was produced for each of the phase images. By dividing each of phase images $\Delta\phi_i$ with its respective product $C_E t_i$, images representing the different potentials for the energy filtered and unfiltered defocus series was obtained. The potential line profiles given in Figure 6.10, are taken from the regions of their respective phase image presented in Figure 6.7.

Figure 6.10 shows that the mean inner potential of Cu_2O is clearly affected by applying an energy filter. The profile given by the unfiltered defocus series suggest an increasing potential

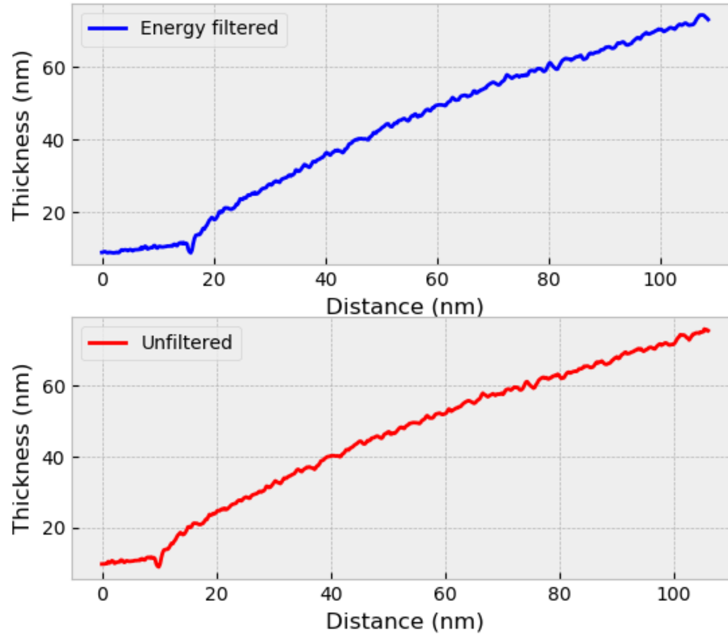

Figure 6.9: *Thickness profiles of Cu_2O. The figures is made along the direction pointed out by the arrow in Figure 6.7, and the profile was made by the average value of the width (100 pixels) of the region outlined in the same figure.*

that does not seem to converge until deep into the sample, if at all. On the other hand, the energy filtered potential profile looks to have stabilized with a mean inner potential of 14.04±0.89 V. The slope of both potential profiles may be due to surface effects, since, close to the edge of the sample the bulk to surface ratio becomes small. By investigating the phase profiles, both show a linear trend, indeed, the energy filtered profile seems to have a slight dip around 80 nm, that might explain the dip in the potential profile, and may indicate that the potential has not stagnated and shows the same increasing trend as the unfiltered profile.

However, investigation of the upper thickness profile in Figure 6.9 revealed that the profile in vacuum does not behave as expected. In vacuum the thickness profile should be zero due to the definition of the log ratio method given above in equation (6.1), where $I_t/I_0 = 1$. To correct for this error, the average value of 9.73 nm from the thickness in vacuum was subtracted from the entire thickness image. A comparison between the original thickness and the corrected thickness is found in Figure 6.11.

With a corrected thickness map, the same procedure as explained above was used to produce a new potential profile of the energy filtered series, given in Figure 6.12. The profile shows signs of noise close to the vacuum region as the values there are close to zero.

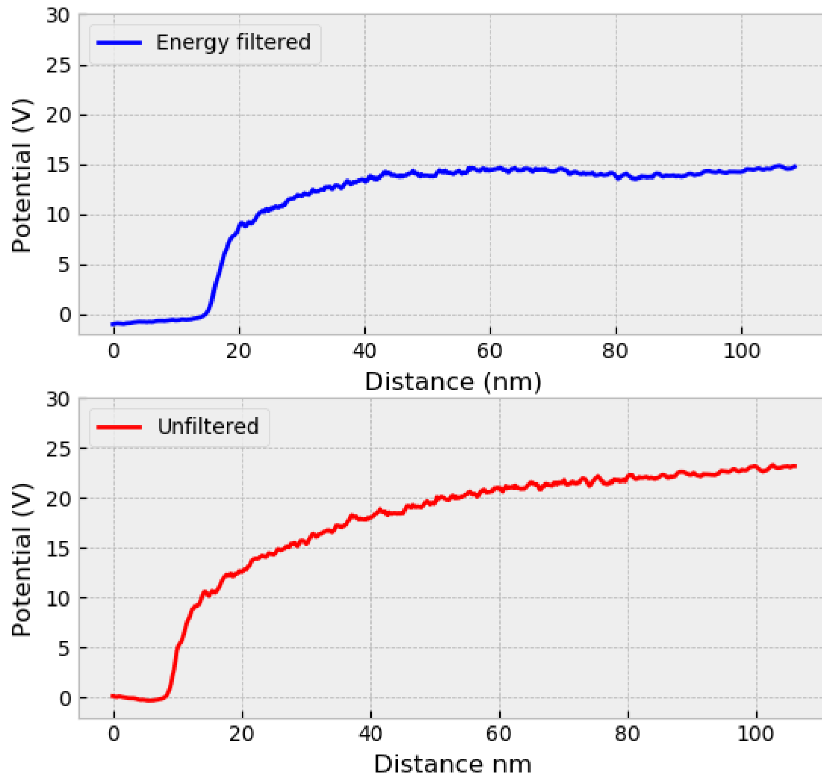

Figure 6.10: *Potential profile made from the energy filtered (top) and unfiltered (bottom) defocus series from averaging over a 100 pixels wide region. The region used to produce for the top profile is presented in the left image in Figure 6.7 and the bottom profile is produced by the region shown in the right image of the same figure.*

This gives a mean inner potential of 16.89±1.29 V, which is 2.9 V higher than the first estimated. This leads to an average of the two estimates of 15.46 V. The previously calculated values for Cu_2O are 17.29 V using the unbinding atom model, and 12.78 V for the fully ionized atom model. Both experimental results found lies between the two theoretically calculated.

However, the source of the error in the thickness profile is still unknown, which makes the results highly uncertain. and the correction method chosen here is highly rudimentary. An alternative explanation may lie in the hardware of the TEM, as there was problems with the CCD over heating during the experiment. For a more accurate measurement of the mean inner potential of Cu_2O, these problems must be resolved.

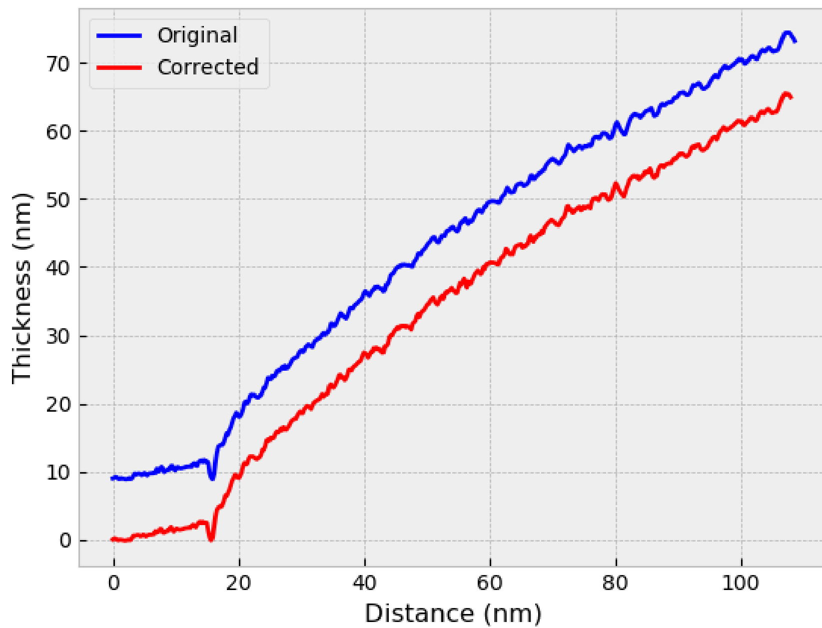

Figure 6.11: *Profiles of the thickness before and after correcting the original thickness image by subtracting the mean of the thickness observed in the vacuum region.*

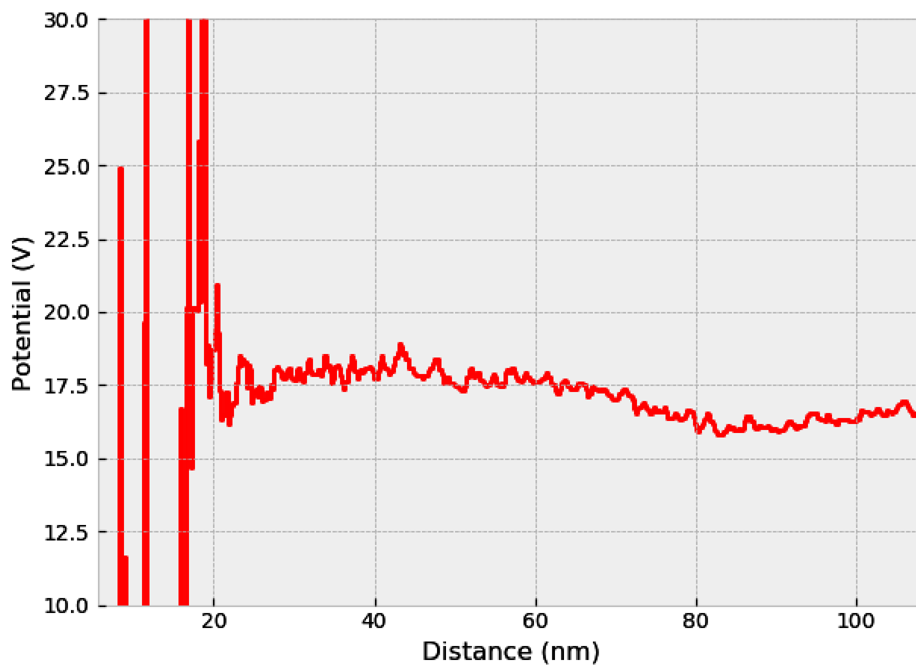

Figure 6.12: *Mean inner potential profile made from the thickness corrected image. The part up to about 20 nm is caused by the software, as it compensates for dividing by numbers close to zero in the region close to and in vacuum.*

6.5 Measurements of potentials in a Cu_2O/CuO/ZnO heterojunction

Measurements of the potential profile across a Cu_2O/CuO/ZnO layered structure were conducted using the JEOL2100F microscope. The 5 nm CuO layer is a nice feature to study and to the authors knowledge it has not been studied by holography before. The sample was provided by S. Gorantla and has been the subject of a larger, previous, study reported in references [53–55]. The TEM is equipped with a Gata Imaging Filter (GIF) and the defocus series was acquired through the GIF with a magnification of x12k, corresponding to an actual magnification of about x180k. A high contrast objective aperture of 20 μm was employed, isolating the central spot. This was done after tilting the sample out of zone-axis with respect to the ZnO layer, the tilt was mainly along the interface. The geometry of the sample and an overview of the area investigated are given in Figure 6.13.

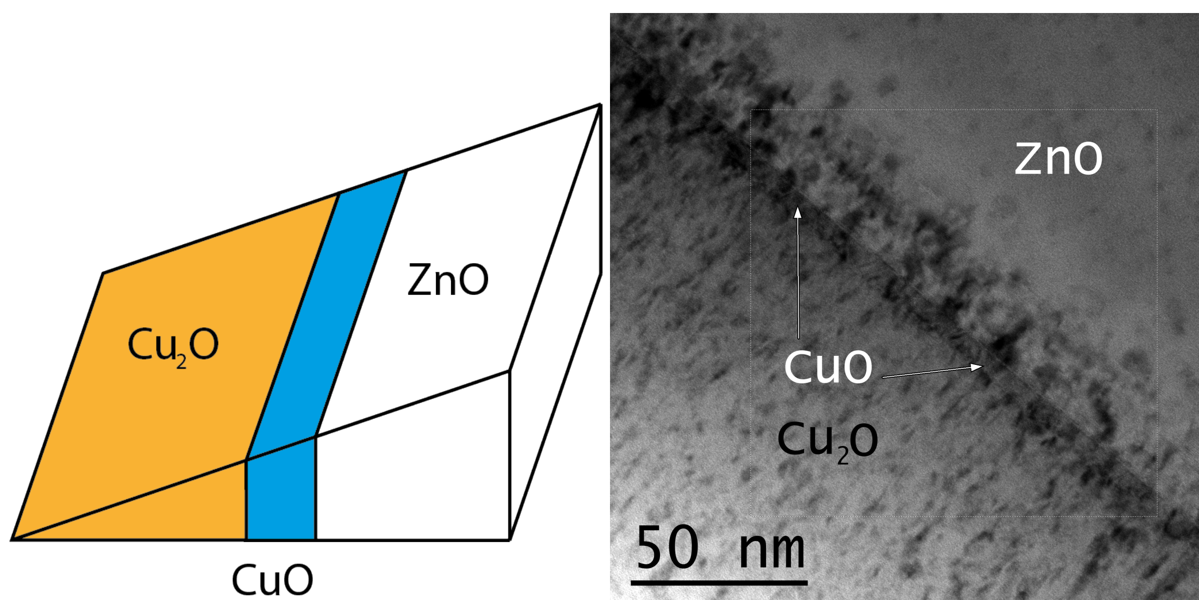

Figure 6.13: Schematics of the sample geometry is shown to the left. Overview image of the region chosen to make a focal series is shown to the right. The sample consist of a Cu_2O and ZnO layer with an intermediate CuO layer between the two as indicated by the arrows. The square region represents the region chosen to be used in reconstruction process.

The defocus series was made using the FRWR software described in the introductory section of this chapter. Using a defocus step size of 30 nm, a total of 15 images was acquired using quadratic defocus increments. Additionally, the defocus series was energy filtered with an energy selecting slit width of 10 eV, centered about the zero loss region. The combination of the

GIF energy filtering and the objective aperture gave a very low intensity, each of the images was taken with a 15 s exposure time to compensate for this. A mean free path (m.f.p.) image of the same region was also produced. This was done by the log ratio method, using an energy window of 10 eV, directly after obtaining the focal series.

The reconstruction of the defocus series yielded the relative phase image presented in Figure 6.14. As there is no vacuum reference, the phase is relative. The different regions show clearly distinct values. A line profile, averaged over the 350 pixel width of the indicated area outlined in Figure 6.14, is presented in Figure 6.15.

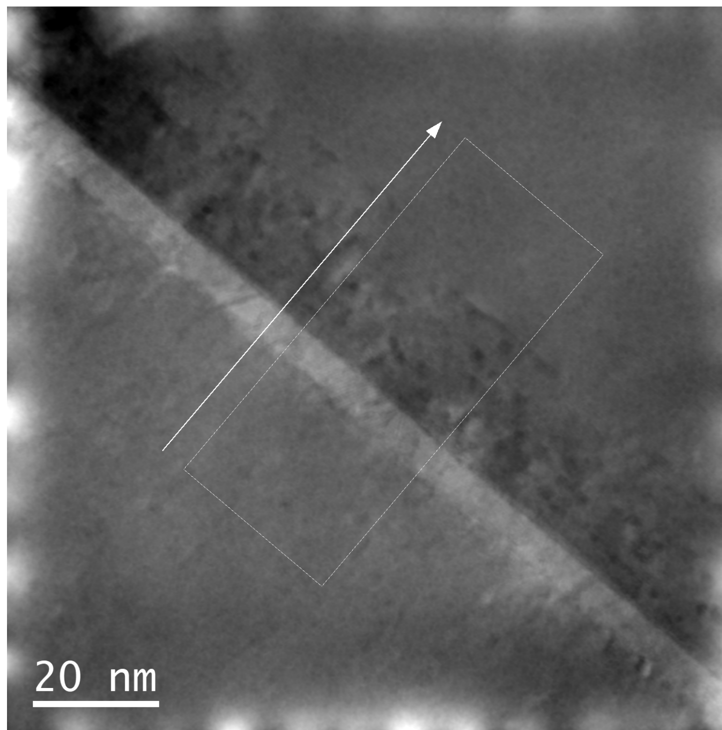

Figure 6.14: *Phase image of Cu_2O\CuO\ZnO going from lower left to upper right. The indicated area corresponds to the profile shown in Figure 6.15.*

From the m.f.p. image given in Figure 6.16, the line profile presented in Figure 6.17 was produced by averaging over the width (350 pixels) of the region illustrated in Figure 6.16.
The different materials considered here, have different inelastic m.f.p. values. These are given in Table 6.1, and was calculated using the method formulated by Malis et al. [57]. The different inelastic mean free path values pose a problem when calculating the thickness across the three materials.
Assuming that the thickness behaves linearly, two thickness estimates were extrapolated from the slopes of Cu_2O and ZnO regions. This was done by least squares regression of the two regions outlined or marked in Figures 6.16, 6.17 and 6.18. The regression analysis for Cu_2O

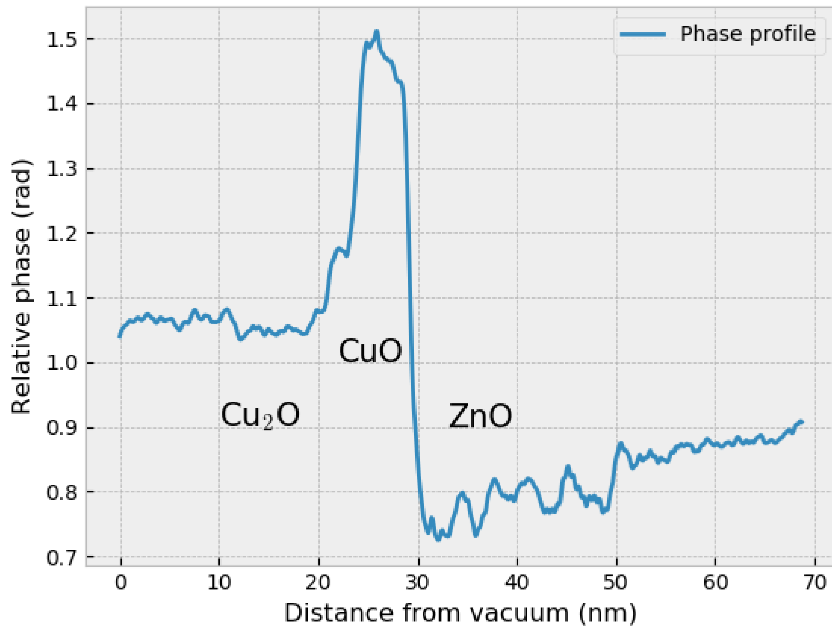

Figure 6.15: *Profile of indicated area in Figure 6.14. The area indicated in Figure 6.14 has a width of 350 pixels; the profile shows their average value.*

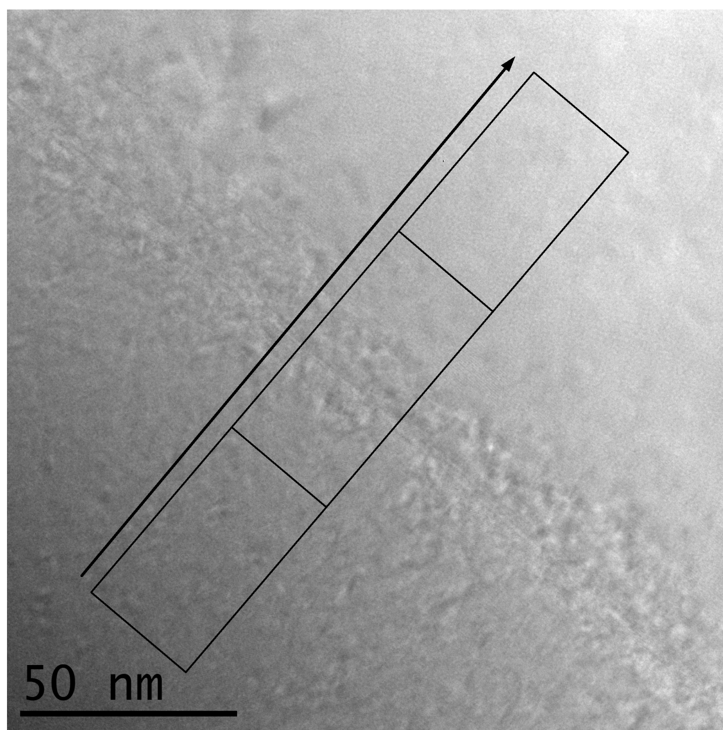

Figure 6.16: *The thickness per mean free path image made by the log ratio method. The region indicated has a width of 350 pixels and is the basis for the line profile presented in Figure 6.17.*

Table 6.1: *Calculated inelastic mean free path by the Malis [57] method by the script provided by Mitchell [58]. Calculations done for β = 157 mrad and 200kV high tension. For further discussion on the mean free path, see appendix D.*

	Cu_2O	CuO	ZnO
λ_i	71.61	75.62	74.99

was made based on the t/λ_i data points presented in Figure 6.17, taking all points starting from the left ending on the first vertical line at 50 nm. This yielded the extrapolated red dashed line given in Figure 6.18. The regression analysis of ZnO was done in the same manner, starting from the second line at 110 nm presented in Figure 6.17 and ending with the last data point of the same figure, resulting in the blue dotted line in Figure 6.18.

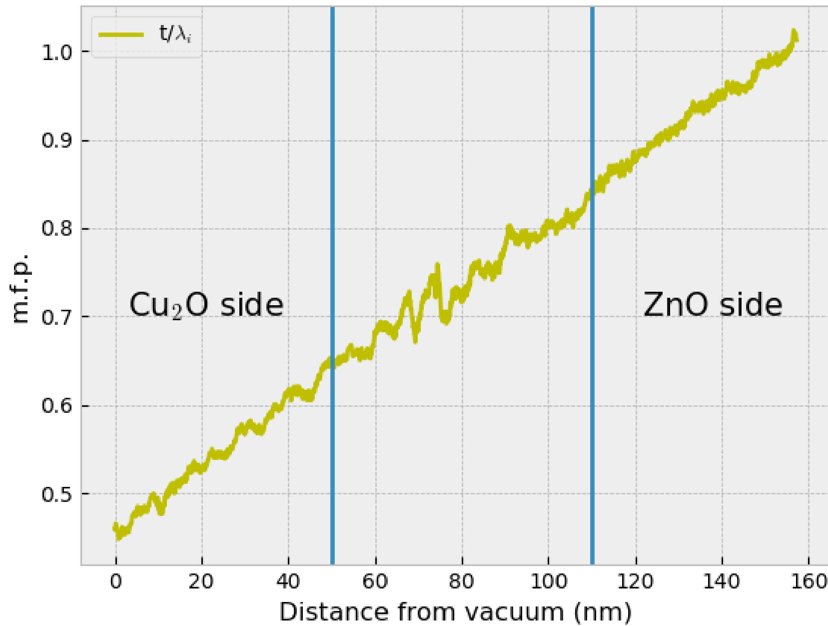

Figure 6.17: *Line profile made by the average of the width (350 pixels) across the region indicated in Figure 6.16. Going from left to right, the vertical lines marks the stop and start points for the linear regression used to extrapolate the lines shown in Figure 6.18*

From the two extrapolated m.f.p. lines a set of thickness profiles was produced by multiplying each extrapolated line by its respective inelastic mean free path. The result of this is presented in Figure 6.19. By multiplying the thickness profiles with the interaction constant C_E, and dividing the phase profile by each of the products mentioned, the two relative potential profiles given in Figure 6.20 was produced.

To measure the potential with uncertainty, the mean and standard deviation of the phase was extracted from the phase image from three 1 nm wide regions, marked with dotted lines in

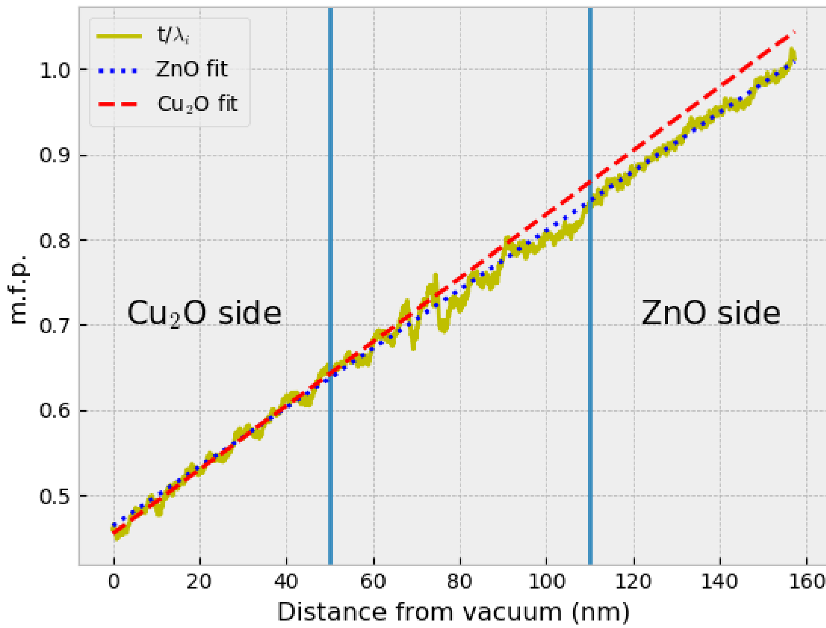

Figure 6.18: *Line profile of the thickness per mean free path (t/λ_i) shown in yellow. The dashed lines are made by least square extrapolation. The red Cu_2O line was extrapolated using the (t/λ_i) up to the 50 nm mark. The blue ZnO line was extrapolated from the 110 nm mark to the end of the (t/λ_i) data points.*

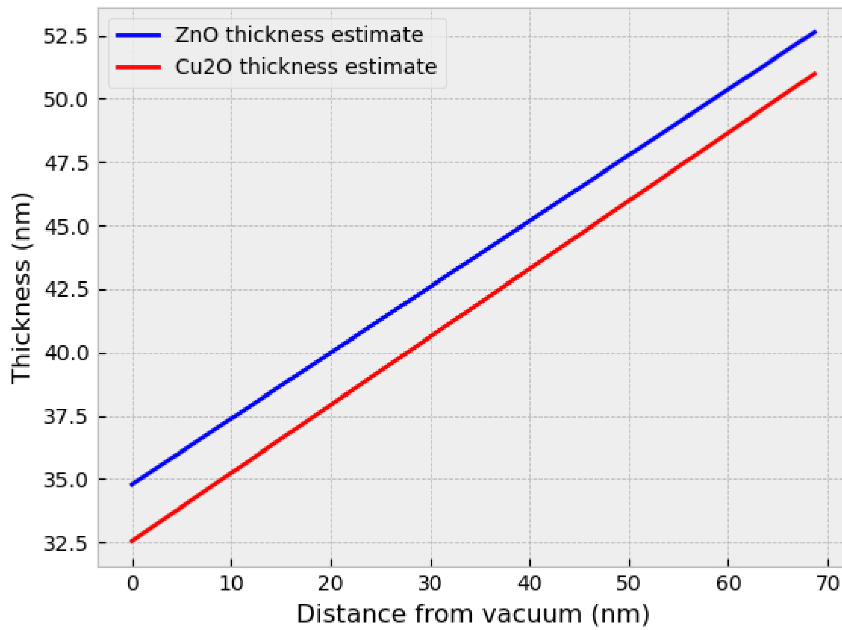

Figure 6.19: *Thickness profiles made by linear regressions of the t/λ_i profile of Figure 6.17 for Cu_2O and ZnO. Profiles are made by multiplying the extrapolated lines by their appropriate λ_i values.*

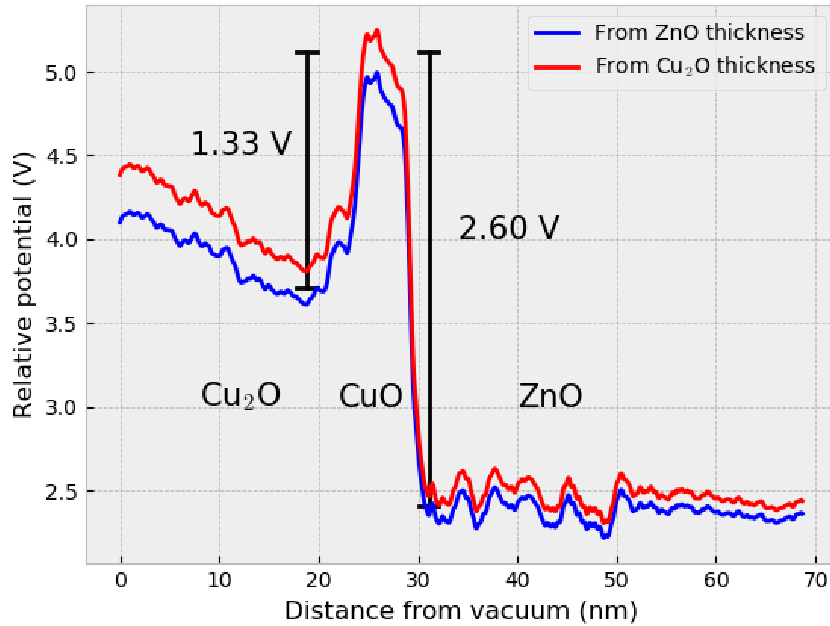

Figure 6.20: *The potential profiles produced from division of the phase profile by the product of the thickness profiles and interaction constant* C_E *= 0.007288rad(nmV)*$^{-1}$*.*

Figure 6.21. As seen in the figure, two of the regions were selected as close to the interface as possible, while the middle region was selected in middle of the CuO layer. By measuring the phase in the three regions, and divide by the average value of the two thickness profiles in the same regions, the potential differences across the two interfaces was found.

The Cu_2O-CuO interface has an average potential jump of 1.33±0.70 V. Considering the differences in the theoretically calculated values for Cu_2O and CuO, a value of 0.98 V was found for the neutral atom model, and for the ionic atom model a value of 2.64 V was calculated. From the CuO to ZnO transition, the profiles show an average potential drop of 2.60±0.84 V. And the difference of CuO-ZnO from the theoretically calculated values give a value of 3.13 V with the neutral atom model and 2.34 V for the ionic atom model. The experimental values from both interfaces lie in the range of the theoretical values, suggesting that the experimental values are reliable. It should also be mentioned that the thickness estimations gives additional spread in the certainty of the experimental potential values.

Both profiles show a shoulder in the Cu_2O/CuO transition of about 0.3 V height and 4.1 nm width. This feature may be explained by an accumulation of positive charge on the Cu_2O/CuO interface, resulting in a higher potential detected. The total peak, including the shoulder, has a width of about 12 nm, which is more than double of the earlier reported [53–55] width of

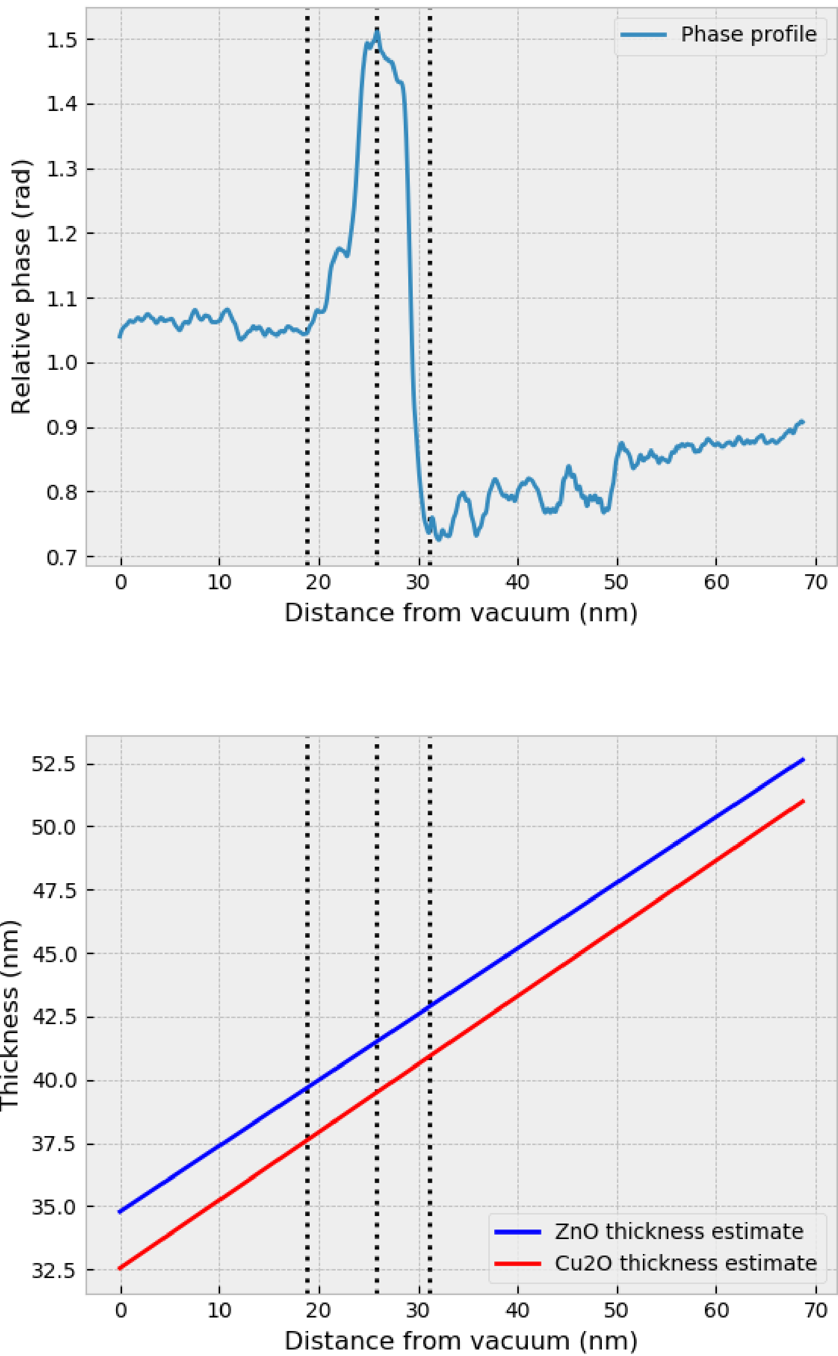

Figure 6.21: *Illustrating the different regions used to calculate the spread of the potential differences. The top shows the phase profile. The lines crossing the phase profile indicate the center of a 1 nm region, where the mean and standard deviation was calculated from the phase image. The bottom presents the thickness estimates where the width is the same as used for the phase estimates. The average of the two thicknesses crossing a black line was used as the thickness to calculate the potential difference in the three regions.*

the CuO layer. This might indicate the existence of a depletion region. A further investigation of the exact position of the peak in relation to the CuO layer reveals that the full width at half maximum of the peak relates to the width of the clearly observed CuO layer in the phase image. This is shown in Figure 6.22. The width of the peak and shoulder may also suggests that the sample was tilted in the direction perpendicular to the CuO layer.

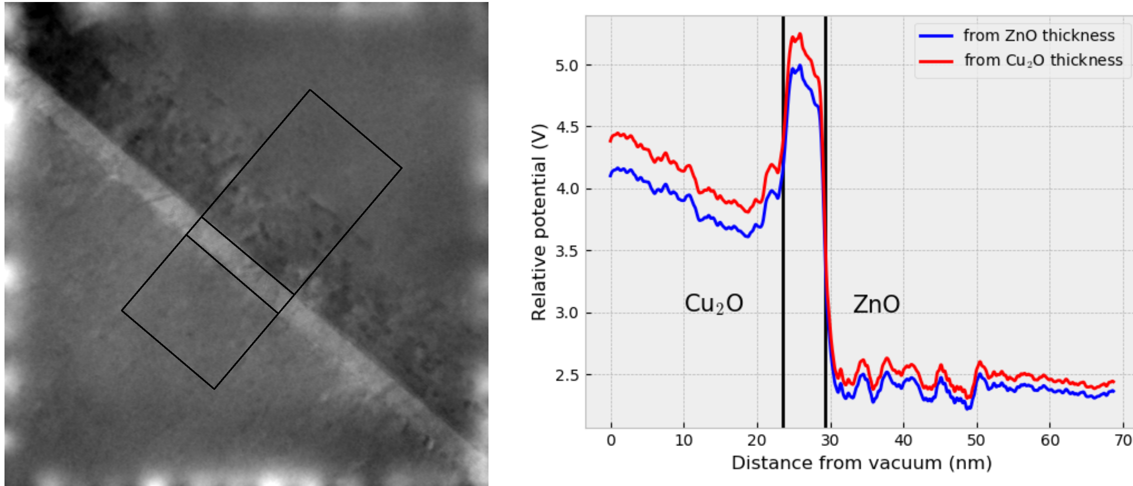

Figure 6.22: *Phase image illustrating (left) containing the indicated regions marked with black lines in the figure to the right. Illustrating the the full width at half maximum of the potential peak lies on the CuO layer.*

The gap between the two potential profiles decrease as the thickness increase. This may be explained by the different slopes of the to fitted thickness. The slope of the potential profiles, Cu_2O region, is caused by the division of the thickness as the phase profile has seemingly flat region in the Cu_2O. However, the ZnO region of the phase has a slight slope, which is counteracted by the division of the thicknesses, as seen in Figure 6.15. As the following expression,

$$\phi = C_E t V_0, \tag{6.3}$$

gives a linear relation between the phase and the thickness, it is surprising that the phase does not show a larger gradient overall. The reason for this may be that the gradient flipping part of the FRWR algorithm, suppressed too much of the low spatial frequencies of the phase such that the true gradient, due to thickness, is lost. Reconstruction with no gradient flipping gave a phase profile that was unsatisfactory as it had negative phase values around a main peak, without any sign of a slope corresponding to the thickness profile.

The extrapolated lines of the thickness estimates from Figure 6.19, show a difference between the Cu_2O and ZnO starting at 2.5 nm before reducing to 1.5 nm. This may be explained by the difference in the extrapolated slopes from the m.f.p. measurement. As the last step for the sample preparation was ion milling, a difference in sputtering rate between the Cu_2O and ZnO may explain the different slopes. For a more exact thickness measurement, this challenge must be overcome.

Chapter 7

Conclusions and suggestions for future work

In this thesis the effects of energy filtering and objective aperture on the output from the FRWR algorithm was investigated. In addition, the mean inner potential of Cu_2O, and the potential profile across a Cu_2O/CuO/ZnO heterojunction, was measured.

The results from investigations with and without an objective aperture revealed that the objective aperture plays a significant role in reducing ghost like features arising from diffraction effects. Thus, the objective aperture is essential for the reconstruction process to be successful. However, for experiments done using low magnifications around 80 kx and below, a too small aperture will limit the low spatial frequencies, hence, a balance between magnification and objective aperture must be found. From investigating the phase profile of Cu_2O with and without energy filtering, we see that the phase is clearly affected. This indicates that the energy filter should be applied in order to obtain a reasonable phase, which in turn is needed to obtain a reasonable mean inner potential.

The mean inner potential of Cu_2O was found to have an experimental value of 15.46 ± 2.18 V. In addition, theoretical values for the Cu_2O mean inner potential, using two different atom models, was found to be 17.29 V for a neutral atom model and 12.78 V for a ionic atom model. Thus, the experimentally obtained value lies between the two theoretically calculated values.

Experimental investigation of the potential across a Cu_2O/CuO/ZnO heterojunction revealed that the Cu_2O/CuO interface has a potential jump of 1.33 ± 0.70 V. In comparison, the theoretically calculated values for the Cu_2O/CuO interface was 0.98 V for the neutral atom model

and 2.64 V for the ionic atom model. The CuO/ZnO interface had an experimentally observed potential drop of 2.60±0.84 V, where the theoretically calculated values was 3.13 V for the neutral atom model and 2.34 V for the ionic atom model. Both of the experimental values are in the range of the the corresponding theoretical values, which may indicate that the experimental values are reliable.

The potential barrier had a width of about 12.25 nm, which is larger than the reported 5 nm width of the CuO intermediate layer. This may indicate the existence of a depletion layer on either one, or both, sides of the interface. In addition, the Cu_2O/CuO profile revealed a shoulder, 0.37 V high and 3.20 nm wide, which may indicate that there exist a some charge accumulation on that interface. However, both the shoulder and depletion layer may also be explained by the sample having a tilt that disturbs the measurements.

Based on the observations made in this study we recommend the following for further studies:

- The experimental errors reported here are rather large, and further studies should be preformed to verify all results to gain a more quantitative understanding of the mean inner potential of Cu_2O, and the Cu_2O/CuO/ZnO heterojunction.

- A comparison study using off-axis holography will help to verify the exact value for the mean inner potential of Cu_2O, as off-axis has direct access to a reference wave.

- A recurring problem has been the thickness profile measurements. Alternative methods for determining the thickness across interfaces should be investigated to gain more accurate thickness measurements.

- The effects of the gradient flipping must be investigated further in order to better understand its effect on the observed relative potential values. This may be done through experimenting with the different parameters of for the FRWR algorithm.

- The potential differences relates to electric fields and thus the charge density across the Cu_2O/CuO/ZnO heterojunction and will be connected to bandbending at the junctions. Calculation for these properties should reveal more about the electronic properties of the heterojunction.

Appendices

Appendix A

Measuring the Objective aperture size

Objective lens

On both the microscopes used the objective lens is a so called ultrahigh resolution objective lens (UHRL). In such a lens the two pole pieces sits closer together so that the scattered object wave enters the lower pole piece at a smaller distance than that of other lenses, reducing the spherical aberration.

Associated with the UHRL is a high contrast objective aperture (HCAp), this sits just below the back focal plane (BFP) of the UHRL, contrary to other objective apertures that sit directly in the BFP. This is due to the special arrangement of the pole pieces. As the position of the HCAp is outside of the BFP, it is visible in the image plane as a disc of bright contrast surrounded by dark contrast.

On the TEMs used in this thesis, the HCAp has 4 different aperture sizes, ranging from 120 μm to 5 μm. The purpose of the HCAp is to limit the scattered electrons caused by the object. It does so by limiting parts of the back focal plane. This is most commonly used to enhance contrast or do bright field and dark field imaging [13, 33].

Objective aperture measurements

Using pre-callibrated image-processing software Gatan DigitalMicrograph (DM), the reciprocal d-spacing (d) for each HCAp was extracted, by the use of diffractograms taken of each aperture blocking parts of reflections from a known material. The diffractograms was obtained using electrons with wavelength λ = 2.51pm (200keV).

The calibration of the software was confirmed by verifying that the distances for each reflection correspond with literature. All results from the measurements of the HCAp from Berln and Oslo are displayed in table A.1.

For the JEOL2200FS microscope in Berlin the HCAp measurements was carried out and provided by the Dr. Holm Krimse, investigating diffractograms of GaAs[110] at a camera length of 100cm. The distance from (00$\bar{8}$) to (008) reflections was measured to 0.0357nm, this corresponds to 1/8 of the (002) lattice plane distance i.e. d_{002}^{exp} = 0.2859. The literature gives d_{002} = 0.2827nm. GaAs has a cubic crystal structure so the interpretation of the (002) d-spacing is as 1/2 of the real space distance a. In conclusion the calibration of the Berlin DM is within an error of 1$\%$.

In Oslo the measured HCAp of the JEOL2100F microscope was carried out by the author of this theses, using ZnO[001] which have a hexagonal crystal system. The relation between the lattice plane distance $d_{h,k,l}$, and real space distances a and c is

$$d_{hkl} = \frac{1}{\sqrt{\left(\frac{4}{3a^2}\right)(h^2 + k^2 + hk) + \left(\frac{l}{c}\right)^2}}. \tag{A.1}$$

Investigating the ($\bar{3}$00) to (300) distance, gave 1/6 of the (100) lattice plane distance. This resulted in an experimental d-spacing of d_{100}^{exp} = 0.283nm. Equation (A.1) gave a = 0.327nm, compared with a literature value of a = 0.325nm gives to an error within 1$\%$ for the Oslo DM.

Table A.1: *High contrast objective aperture values measured as explained above for JEOL2100F and JEOL2200FS.*

	Physical size [μm]	Reciprocal size [$1/nm$]	Angular range [$mrad$]
JEOL2100F	120	29.03	72.81
Oslo	60	15.07	37.80
	20	5.61	14.07
	5	1.60	4.01
JEOL2200FS	120	29.40	73.80
Berlin	60	14.90	37.30
	20	5.23	13.10
	5	1.42	3.50

Appendix B

Measuring the modulation transfer function

To obtain the MTF of a certain CCD, a set of images of the closest possible object to the CCD needs to be acquired.

There exist several ways of measuring the MTF, such as the knife edge method [59], where an object is placed directly on top of the CCD to be take images of. These images are then processed to get the MTF fitting parameters. The mentioned method is not optimal as it involves opening the microscope multiple times to place and retrieve the object. However, there exist a method where an aperture may be used instead of the physical object [46].

For the JEOL2100F microscope in Oslo Science park a set of 100 images of the Gatan imaging filter (GIF) entrance aperture was acquired using a CCD with $\Delta_{px} = 14\mu m$. Each image acquired at half of maximum intensity for 2 seconds exposure time. One image without the entrance apperture was also acquired to locate any dead pixels. A simple MATLAB script was produced to remove dead pixels, before sending all images through a findMTF script which was provided by Van Den Broek et al. [46]. Then the mean of all MTF results was taken and used to generate the fitting parameters by equation (5.13). The results of the fitting is shown in figure B.1. As the first fit gave a starting value above 1, which is unphysical, a different fit using $C = (1 - A)$ was used to make ensure a physical starting value.
The fitting parameters used in FRWR along with the unphysical fit are displayed in Table B.1, along with the interval width for the parameters used with a 95% confidence level.

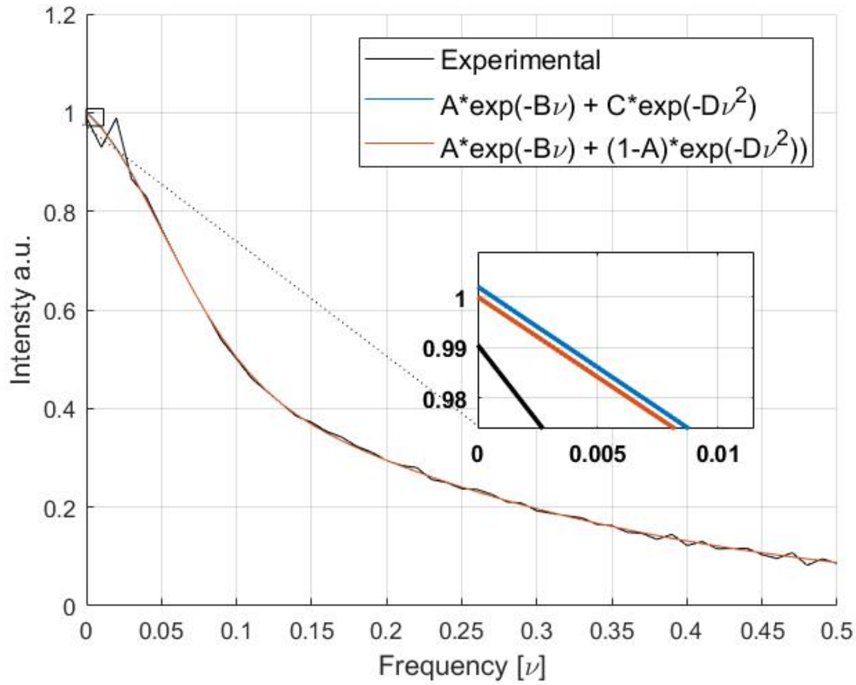

Figure B.1: *Plot showing MTF mean from 100 images taken of GIF entrance aperture on JEOL2100F in black. Fit for FRWR using eq.* (5.13) *in blue and the fit constricting the MTF to a value of 1 for a frequency of 0 shown in orange.*

Table B.1: *Showing fitting parameters obtained using a confidence level of 95% along with the interval widths of all parameters.*

Fitting parameters	A	B	C	D
$Ae^{-B\nu} + Ce^{-D\nu^2}$	0.6612	4.041	0.3408	170.9
Interval width	0.0724	0.422	0.0668	42.7
Used fit ($C = 1 - A$)	0.6592	4.031	0.3408	196
Interval width	0.0662	0.391	0.0662	32.6

Appendix C

Energy Filtered Transmission Electron Microscopy

As electrons interact with a sample they may partake in inelastic interactions, that result in a loss of the kinetic energy from the electron to the sample. This energy loss occurs mainly due to the creation of plasmons, which are oscillations in the electron cloud of the material, and excitations of electrons bound to the core of the atom nucleus. Electrons that have lost energy complicates the interpretation of the phase as discussed in section 3.2.2.

By the use of energy filtered TEM (EFTEM) the inelastic electrons are removed. This is accomplished by applying a magnetic field, **B**, perpendicular to the electron beam. Due to the Lorentz force, the electrons will disperse according to their velocity, **v**, into a spectrum of electrons. By applying a filter to the spectrum, one may effectively collect electrons with a desired energy loss. The Lorentz force is given as

$$F_{Lorentz} = q(\mathbf{v} \times \mathbf{B}). \tag{C.1}$$

There are two different types of energy filters, the Gatan Image Filter (GIF) and the Ω-filter. A brief explanation of the different energy filters will here be given.

Gatan imaging filter uses what is called a magnetic prism that disperse the electrons as illustrated in Figure C.1. The alignment coils allows for adjustment of the spectrum by applying a bias, the energy slit width and position are adjusted to collect electrons with a desired energy

loss.

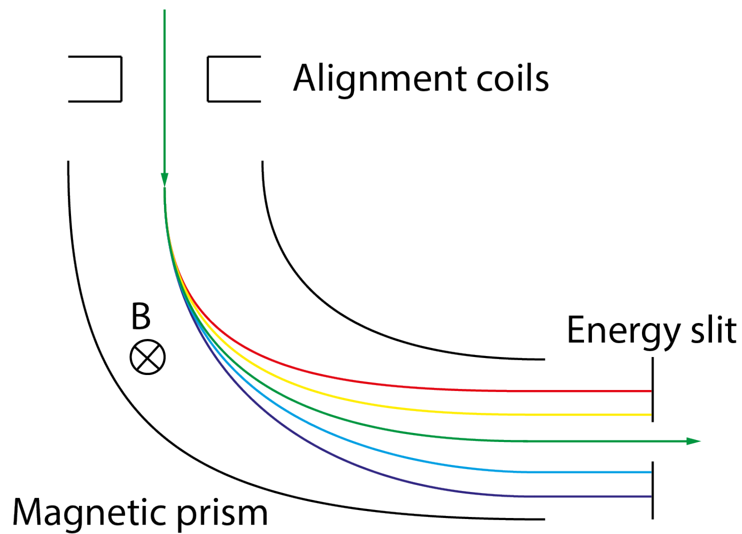

Figure C.1: *The Gatan imaging filter separates electrons according to energy so that the inelastic electrons may be filtered out.*

The GIF sits at the bottom of the TEM column and sends electrons through an extra set of lenses to focus the energy filtered electrons on to a detector that increases the effective camera length and magnification of the microscope. For the JEOL2100F used in this thesis, this magnification is about 15 times the magnification displayed on the fluorescent screen.

The Ω-filter entrance sits between the last intermediate lens and first projector lens in the TEM column and bends the electrons as illustrated in Figure C.2. The electrons are bent in a symmetric fashion: this disperse them into a spectrum projected on to an adjustable energy selecting slit. The JEOL2200FS used in in this thesis is equipped with an Ω-filter.

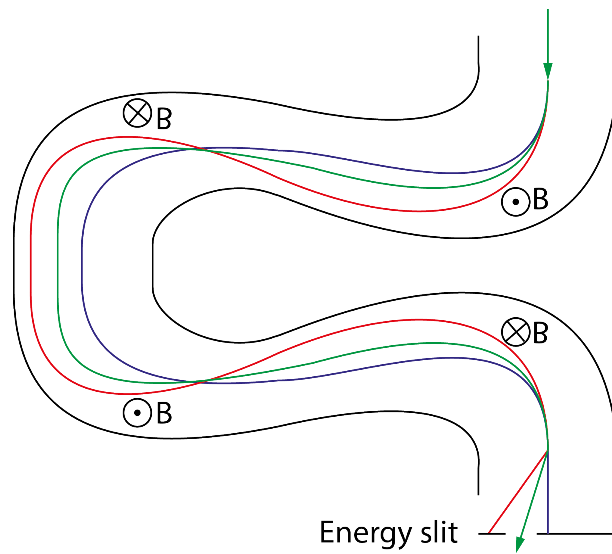

Figure C.2: *Electrons are bent going through the* Ω*-filter and exits the filter in a spectrum that may be filtered according to the energy loss.*

Appendix D

The log ratio method for thickness measurements

The log ratio method [56, p. 294] is a common method for estimating the thickness of a TEM sample. It is derived from Poisson's law under the assumption that the number of scattering events are small. The log ration is given by is

$$\frac{t}{\lambda_i} = \ln(\frac{I_t}{I_0}), \tag{D.1}$$

and it relates the thickness t to the total inelastic electron mean free path λ_i. λ_i is dependent on the aperture limiting the electron scattering angle $\Delta\mathbf{k}$. The total intensity is I_t, and the zero energy loss intensity I_0. According to Malis et al. [57], this formulation is within $\pm 20\%$ accuracy for most inorganic samples, if the correct λ_i is known.

There are two analytic methods to calculate λ_m known to the author. The first method was realized by Lakoubovskii et al. [60]. The second produced by Malis [57] is given by

$$\lambda_i \approx \frac{106\gamma E}{E_m \ln(2\beta E/E_m)}, \tag{D.2}$$

$$\tag{D.3}$$

where E is the incident electron energy, β the collection semi angle, γ the relativistic Lorentz factor, and the experimental fitting variable E_m is based on the atomic number Z. This results

in an expression for λ_i. The experimental fitting variable was estimated for incident energies of 80 to 100 keV to be [57]

$$E_m \approx 7.6Z^{0.36}. \tag{D.4}$$

And for materials consisting of several elements the following estimation may be done [56, p. 297],s

$$Z_{eff} \approx \frac{\sum_i f_i Z_i^{1.3}}{\sum_i f_i Z_i^{0.3}}. \tag{D.5}$$

D. R. G. Mitchell [58] have created a GATAN DigitalMicrograph script for estimating the inelastic mean free path using either of the methods mentioned above. The different mean free paths used in this thesis was calculated by the mentioned DM plugin, and are presented in Table D.1.

Table D.1: *Calculated inelastic mean free path by the Malis [57] method by the script provided by Mitchell [58]. Calculations done for β = 157 mrad and 200kV high tension.*

	Cu_2O	CuO	ZnO
λ_i	71.61	75.62	74.99

Bibliography

[1] D. Gabor. A New Microscopic Principle. *Nature*, 161(4098):777–778, 15 May 1948.

[2] C. T. Koch. Towards full-resolution inline electron holography. *Micron*, 63:69–75, 2013.

[3] C. T. Koch. A flux-preserving non-linear inline holography reconstruction algorithm for partially coherent electrons. *Ultramicroscopy*, 108(2):141–150, 2008.

[4] K. Song, S. Ryu, H. Lee, T. R. Paudel, C. T. Koch, B. Park, J. K. Lee, S. Y. Choi, Y. M. Kim, J. C. Kim, H. Y. Jeong, M. S. Rzchowski, E. Y. Tsymbal, C. B. Eom, and S. H. Oh. Direct imaging of the electron liquid at oxide interfaces. *Nat. Nanotechnol.*, 13(3):198–203, 2018.

[5] J. M. Mánuel, C. T. Koch, V. B. Özdöl, W. Sigle, P. A. Van Aken, R. García, and F. M. Morales. Inline electron holography and VEELS for the measurement of strain in ternary and quaternary (In,Al,Ga)N alloyed thin films and its effect on bandgap energy. *J. Microsc.*, 261(1):27–35, 2016.

[6] D. Abou-Ras, S. S. Schmidt, N. Schäfer, J. Kavalakkatt, T. Rissom, T. Unold, R. Mainz, A. Weber, T. Kirchartz, E. Simsek Sanli, P. A. van Aken, Q. M. Ramasse, H. Kleebe, D. Azulay, I. Balberg, O. Millo, O. Cojocaru-Mirédin, D. Barragan-Yani, K. Albe, J. Haarstrich, and C. Ronning. Compositional and electrical properties of line and planar defects in Cu(In,Ga)Se ₂ thin films for solar cells - a review. *Phys. status solidi - Rapid Res. Lett.*, 10(5):363–375, 2016.

[7] C. Kittel. *Introduction to Solid State Physics*. John Wiley & Sons, Inc., New York, 8th edition, 2005.

[8] B. Fultz and J. M. Howe. *Transmission electron microscopy and diffractometry of materials*. 2008.

[9] A. Tonomura. *Electron holography*. Springer-Verlag, Berlin Heidelberg, 1993.

[10] C. J. Davisson and L. H. Germer. Reflection of Electrons by a Crystal of Nickel. *Proceedings of the National Academy of Sciences*, 14(4):317–322, 1928.

[11] A. Tonomura, J. Endo, T. Matsuda, T. Kawasaki, and H. Ezawa. Demonstration of single-electron buildup of an interference pattern. *American Journal of Physics*, 57(2):117–120, 1989.

[12] R. Bach, D. Pope, S. H. Liou, and H. Batelaan. Controlled double-slit electron diffraction. *New Journal of Physics*, 15, 2013.

[13] B. Fultz and J. M. Howe. *Transmission electron microscopy and diffractometry of materials*. 2008.

[14] D. Rez, P. Rez, and I. Grant. Dirac-Fock Calculations of X-ray Scattering Factors and contributions to the Mean Inner Potential for Electron Scattering. *Acta Crystallographica Section A*, 50:481–497, 1994.

[15] P. Kruse, M. Schowalter, D. Lamoen, A. Rosenauer, and D. Gerthsen. Determination of the mean inner potential in III – V semiconductors , Si and Ge by density functional theory and electron holography. 106:105–113, 2006.

[16] P. A. Doyle and P. S. Turner. Relativistic Hartree–Fock X-ray and electron scattering factors. *Acta Crystallographica Section A*, 24(3):390–397, 1968.

[17] A. Sanchez and M. A. Ochando. Calculation of the mean inner potential. *J. Phys. C Solid State Phys.*, 18(1):33–41, 1985.

[18] J. F. Menadue. Si(111) surface structures by glancing-incidence high-energy electron diffraction. *Acta Crystallogr. Sect. A*, 28(1):1–11, 1972.

[19] M. Elfwing and E. Olsson. Electron holography study of active interfaces in zinc oxide varistor materials. *J. Appl. Phys.*, 92(9):5272–5280, 2002.

[20] J. Taftø. Personal communication.

[21] D. K. Saldin and J. C.H. Spence. On the mean inner potential in high- and low-energy electron diffraction. *Ultramicroscopy*, 55(4):397–406, 1994.

[22] M. De Graef and Z. Yimei. *Magnetic imaging and its applications to materials*, volume 36. Academic Press, 2001.

[23] Y. Aharonov and D. Bohm. Significance of Electromagnetic Potentials in the Quantum Theory. *Physical Review*, 115(3):485–491, 1959.

[24] A. T, T. Matsuda, T. Kawasaki, J. Endo, S. Yano, and H. Yamada. Evidence For Aharonov-Bohm Effect With Magnetic Field Completley Shielded From Electron Wave. *Physical review letters*, 24(8):792–795, 1986.

[25] M. De Graef and Z. Yimei. *Magnetic imaging and its applications to materials*, volume 36. Academic Press, 2001.

[26] G. Möllenstedt and H. Düker. Beobachtungen und Messungen an Biprisma-Interferenzen mit Elektronenwellen. *Zeitschrift für Physik*, 145:377–397, 1956.

[27] J. M. Cowley. Twenty forms of electron holography. *Ultramicroscopy*, 41(4):335–348, 1992.

[28] C. T. Koch, S. Bhattacharyya, M. Rühle, Raphaëlle L. Satet, and M. J. Hoffmann. Measuring electrostatic potential profiles across amorphous intergranular films by electron diffraction. *Microsc. Microanal.*, 12(2):160–169, 2006.

[29] A. M. Maiden, M. C. Sarahan, M. D. Stagg, S. M. Schramm, and M. J. Humphry. Quantitative electron phase imaging with high sensitivity and an unlimited field of view. *Sci. Rep.*, 5:1–8, 2015.

[30] R. W. Gerchberg and W. O. Saxton. A practical algorithm for the determination of phase from image and diffraction plane pictures. *Optik (Stuttg).*, 35(2):237–246, 1972.

[31] L. J. Allen, W. McBride, N. L. O'Leary, and M. P. Oxley. Exit wave reconstruction at atomic resolution. *Ultramicroscopy*, 100(1-2):91–104, 2004.

[32] S. S. Schmidt. Microscopic properties of grain boundaries in Cu (In , Ga) Se 2 and CuInS 2 thin-film solar cells studied by transmission electron microscopy. 2011.

[33] D. B. Williams and C. B. Carter. *Transmission Electron Microscopy*. 2009.

[34] S. Bhattacharyya, C. T. Koch, and M. Rühle. Projected potential profiles across interfaces obtained by reconstructing the exit face wave function from through focal series. *Ultramicroscopy*, 106(6):525–538, 2006.

[35] M. R. Teague. Deterministic phase retrieval: a Green's function solution. *Journal of the Optical Society of America*, 73(11):1434, 1983.

[36] T. E. Gureyev, A. Roberts, and K. A. Nugent. Partially coherent fields, the transport-of-intensity equation and phase uniqueness. *J. Opt. Soc. Am. A*, 12:1942–1946, 1995.

[37] M. De Graef and Z. Yimei. *Magnetic imaging and its applications to materials*. Academic Press, 1 edition, 2000.

[38] M Ã Beleggia, M. A. Schofield, V. V. Volkov, and Y. Zhu. On the transport of intensity technique for phase retrieval. 102:37–49, 2004.

[39] D. Paganin and K. A. Nugent. Noninterferometric Phase Imaging with Partially Coherent Light. *Physical review letters*, 1998.

[40] K. Nugent, T. Gureyev, D. Cookson, D. Paganin, and Z. Barnea. Quantitative Phase Imaging Using Hard X Rays. *Phys. Rev. Lett.*, 77(14):2961–2964, 1996.

[41] K. Ishizuka and B. Allman. Phase measurement of atomic resolution image using transport of intensity equation. *J. Electron Microsc. (Tokyo).*, 54(3):191–197, 2005.

[42] L. J. Allen and M. P. Oxley. Phase retrieval from series of images obtained by defocus variation. *Opt. Commun.*, 199(November):65–75, 2001.

[43] K. Ishizuka. Contrast transfer of crystal images in TEM. *Ultramicroscopy*, 5(1-3):55–65, 1980.

[44] C. T. Koch. Full-resolution inline electron holography (FRIH). 110(2010):6–7, 2012.

[45] R. R. Meyer, A. I. Kirkland, and W. O. Saxton. A new method for the determination of the wave aberration function for high resolution TEM: 1. Measurement of the symmetric aberrations. *Ultramicroscopy*, 92(2):89–109, 2002.

[46] W. Van den Broek, S. Van Aert, and D. Van Dyck. Fully Automated Measurement of the Modulation Transfer Function of Charge-Coupled Devices above the Nyquist Frequency. *Microscopy and Microanalysis*, 18(02):336–342, 2012.

[47] D. B. Williams and C. B. Carter. *Transmission Electron Microscopy*. 2009.

[48] J. M. Cowley. *Diffraction physics*. North-Holland publishing company, New York, second, revised edition edition, 1981.

[49] A. Parvizi, W. Van den Broek, and C. T. Koch. Recovering low spatial frequencies in wavefront sensing based on intensity measurements. *Adv. Struct. Chem. Imaging*, 2(1):3, 2017.

[50] A. Parvizi, W. Van den Broek, and C.T. Koch. Gradient flipping algorithm: introducing non-convex constraints in wavefront reconstructions with the transport of intensity equation. *Opt. Express*, 24(8):8344, 2016.

[51] A. Parvizi, J. Müller, S. A. Funken, and C. T. Koch. A practical way to resolve ambiguities in wavefront reconstructions by the transport of intensity equation. *Ultramicroscopy*, 154:1–6, 2015.

[52] C. T. Koch. (nonlinear) inline electron holography. `https://www.physics.hu-berlin.de/en/sem/software/software_frwrtools`. Accessed: 2018-05-15.

[53] A. E. Gunnæs, S. Gorantla, O. M. Løvvik, J. Gan, P. A. Carvalho, B. G. Svensson, E. V. Monakhov, K. Bergum, I. T. Jensen, and S. Diplas. Epitaxial Strain-Induced Growth of CuO at Cu2O/ZnO Interfaces. *J. Phys. Chem. C*, 120(41):23552–23558, 2016.

[54] J. Gan, S. Gorantla, S. Diplas, O. M. Løvvik, B. G. Svensson, E. V. Monakhov, and A. E. Gunnæs. Structural properties of Cu₂O epitaxial films grown on c-axis single crystal ZnO substrate by radio frequency magnetron sputtering. *Appl. Phys. Lett.*, 108(2016):152110, 2016.

[55] I. J. T. Jensen, S. Gorantla, S. Diplas, O. M. Løvvik, B. G. Svensson, E. V. Monakhov, and A. E. Gunnæs. Structural properties of Cu₂O epitaxial films grown on c-axis single crystal ZnO substrate by radio frequency magnetron sputtering. *Appl. Phys. Lett.*, 108(2016):152110, 2016.

[56] R. F. Egerton. *Electron Energy-Loss Spectroscopy in the Electron Microscope*. Springer, 3 edition, 2011.

[57] T. Malis, S. C. Cheng, and R. F. Egerton. Log-Ratio Technique for Specimen-Thickness Measurement in the TEM. *J. Electron Microsc. Tech.*, 8:193–200, 1988.

[58] D. R. G. Mitchell. Dave mitchell's digitalmicrograph (tm) scripting website. `http://www.dmscripting.com/meanfreepathestimator.html`. Accessed: 2018-05-10.

[59] R. R. Meyer, A. I. Kirkland, R. E. Dunin-Borkowski, and J. L. Hutchison. Experimental characterisation of CCD cameras for HREM at 300 kV. *Ultramicroscopy*, 85(1):9–13, 2000.

[60] K. Iakoubovskii, K. Mitsuishi, Y. Nakayama, and K. Furuya. Mean free path of inelastic electron scattering in elemental solids and oxides using transmission electron microscopy: Atomic number dependent oscillatory behavior. *Phys. Rev. B*, 77(10):104102, mar 2008.